Monthly Notices of the ROYAL ASTRONOMICAL SOCIETY

MNRAS **545,** 1–22 (2026) https://doi.org/10.1093/mnras/staf2106
Advance Access publication 2025 December 03

The Pandora project – II. How non-thermal physics drives bursty star formation and temperate mass-loaded outflows in dwarf galaxies

Sergio Martin-Alvarez [1★] Debora Sijacki,[2,3] Martin G. Haehnelt,[2,3] Alice Concas [4] Yuxuan Yuan [2,3] Roberto Maiolino [2,5] Risa H. Wechsler,[1,6,7] Francisco Rodríguez Montero [8] Marion Farcy [9] Mahsa Sanati [10] Yohan Dubois,[11] Joki Rosdahl [12] Enrique Lopez-Rodriguez [13,1] and Susan E. Clark [1,6]

[1]*Kavli Institute for Particle Astrophysics & Cosmology (KIPAC), Stanford University, Stanford, CA 94305, USA*
[2]*Kavli Institute for Cosmology (KICC), University of Cambridge, Madingley Road, Cambridge CB3 0HA, UK*
[3]*Institute of Astronomy, University of Cambridge, Madingley Road, Cambridge CB3 0HA, UK*
[4]*European Southern Observatory, Karl-Schwarzschild-Strasse 2, D-85748 Garching bei Muenchen, Germany*
[5]*Cavendish Laboratory, University of Cambridge, 19 J. J. Thomson Avenue, Cambridge CB3 0HE, UK*
[6]*Department of Physics, Stanford University, Stanford, CA 94305, USA*
[7]*SLAC National Accelerator Laboratory, Menlo Park, CA 94025, USA*
[8]*Kavli Institute for Cosmological Physics (KICP), The University of Chicago, IL 60637, USA*
[9]*Institute of Physics, Laboratory for Galaxy Evolution, EPFL, Observatoire de Sauverny, Chemin Pegasi 51, CH-1290 Versoix, Switzerland*
[10]*Department of Physics, University of Oxford, Keble Road, Oxford OX1 3RH, UK*
[11]*Institut d'Astrophysique de Paris, UMR 7095, CNRS and Sorbonne Université, 98 bis boulevard Arago, F-75014 Paris, France*
[12]*Univ Lyon, Univ Lyon1, Ens de Lyon, CNRS, Centre de Recherche Astrophysique de Lyon UMR5574, F-69230 Saint-Genis-Laval, France*
[13]*Department of Physics & Astronomy, University of South Carolina, Columbia, SC 29208, USA*

Accepted 2025 November 19. Received 2025 October 18; in original form 2025 June 3

ABSTRACT

Dwarf galaxies provide powerful laboratories for studying galaxy formation physics. Their early assembly, shallow gravitational potentials, and bursty, clustered star formation histories make them especially sensitive to the processes that regulate baryons through multiphase outflows. Using high-resolution, cosmological zoom-in simulations of a dwarf galaxy from *the Pandora suite*, we explore the impact of stellar radiation, magnetic fields, and cosmic ray feedback on star formation, outflows, and metal retention. We find that our purely hydrodynamical model without non-thermal physics – in which supernova feedback is boosted to reproduce realistic stellar mass assembly – drives violent, overly enriched outflows that suppress the metal content of the host galaxy. Including radiation reduces the clustering of star formation and weakens feedback. However, the additional incorporation of cosmic rays produces fast, mass-loaded, multiphase outflows consisting of both ionized and neutral gas components, in better agreement with observations. These outflows, which entrain a denser, more temperate interstellar medium, exhibit broad metallicity distributions while preserving metals within the galaxy. Furthermore, the star formation history becomes more bursty, in agreement with recent *James Webb Space Telescope* findings. These results highlight the essential role of non-thermal physics in galaxy evolution and the need to incorporate it in future galaxy formation models.

Key words: magnetic fields – radiative transfer – methods: numerical – cosmic rays – galaxies: dwarf – galaxies: formation.

1 INTRODUCTION

Dwarf galaxies are the primary dwellers of small dark matter haloes, characterized by their pervasive abundance and shallow gravitational potential wells. An in-depth understanding of dwarf galaxies remains a pressing concern, as they provide a unique probe of our Λ cold dark matter (ΛCDM) model via their abundance, distribution topology on large scales as well as internal structural properties (e.g. S. Garrison-Kimmel et al. 2014; J. Oñorbe et al. 2015; T. Sawala et al. 2016; J. S. Bullock & M. Boylan-Kolchin 2017; M. Geha et al. 2017; P. Jethwa, D. Erkal & V. Belokurov 2018). In a paradigm where galaxy formation proceeds hierarchically, dwarf galaxies constitute the fundamental building blocks of their more massive counterparts. Consequently, dwarf systems not only serve as simple laboratories to investigate the processes of star formation and baryonic feedback, but also allow exploring the physics at play during the formation of the first galaxies in our Universe (M. Geha et al. 2012; V. Gelli et al. 2020; M. P. Rey et al. 2020; M. Sanati et al. 2020, 2024; I. B. Santistevan et al. 2020; T. A. Gutcke et al. 2022; S. Koudmani, D. Sijacki & M. C. Smith 2022; S. Martin-Alvarez et al. 2023; S. Y. Kim et al. 2024). Their often initially rapid stellar mass growth, shallow gravitational potential wells, simplified environments, and pristine gas reservoirs particularly devoid of metals make them

★ E-mail: martin-alvarez@stanford.edu

unique candidates to investigate the cycle of baryons in galaxies and the intricate interrelation between star formation, galactic winds, and galaxy metallicities.

Star formation is one of the fundamental processes regulating galaxy formation and evolution, not only by converting gas into stars, but also by enriching the ISM with metals. Runaway star formation is believed to be largely thwarted by internal galaxy feedback processes, allowing its self-regulation. In dwarf galaxies, the primary drivers of this feedback include stellar radiation (S. Geen et al. 2015; J. Rosdahl et al. 2015; S. Geen, J. D. Soler & P. Hennebelle 2017; M. Y. Grudić et al. 2021; S. Martin-Alvarez et al. 2023), stellar winds (O. Agertz et al. 2013; Y. A. Fichtner et al. 2024), and supernova (SN) explosions (e.g. S. D. M. White & M. J. Rees 1978; V. Springel & L. Hernquist 2003; Y. Dubois & R. Teyssier 2008; P. F. Hopkins, E. Quataert & N. Murray 2012; R. Teyssier et al. 2013; J. Rosdahl et al. 2017; M. C. Smith, D. Sijacki & S. Shen 2019; S. Martin-Alvarez et al. 2023).

In addition to the local suppression of star formation, these feedback processes are the engines of the baryon cycle, expelling gas into the circumgalactic medium (CGM) and even the intergalactic medium (IGM; A. M. Brooks et al. 2007; J. Chisholm et al. 2015; T. M. Heckman et al. 2015; C. C. Hayward & P. F. Hopkins 2017; Y. Zheng et al. 2024). Crucially, these galactic outflows will shape the properties of the CGM gas as their mass-loading, energetics, and metal enrichment influence the hydrodynamical evolution of CGM gas. This, in turn, will determine whether heating or cooling processes dominate, and the time-scales for the eventual gas re-accretion that further fuels the baryonic and star formation cycle (D. Kereš et al. 2005; P. Ocvirk, C. Pichon & R. Teyssier 2008; J. Tumlinson et al. 2011; A. B. Ford et al. 2014; J. Tumlinson, M. S. Peeples & J. K. Werk 2017; Z. Kocjan et al. 2024).

While observational measurements of galactic outflows are a challenging endeavour (e.g. see a review by S. Veilleux, G. Cecil & J. Bland-Hawthorn 2005 for a discussion on UV absorption lines, low S/N, kinematic complexity and line saturation; and more recently S. Veilleux et al. 2020 for cool outflows), they reveal the ejection of gas from the ISM through winds featuring warm and cold thermodynamical components, for which it is possible to characterize key properties such as the column density and velocity (C. C. Steidel et al. 2010; T. M. Heckman et al. 2015; A. Concas et al. 2019; N. M. F. Forster Schreiber et al. 2019; I. Schroetter et al. 2019, 2021; M. Cherrey et al. 2025). These observations further estimate the dimensionless mass-loading ratio, defined as the rate of outflowing mass per rate of star formation. Higher temperature outflow gas phases inherently entrain higher specific thermal energies, dominating the outflows' energy density (C.-G. Kim & E. C. Ostriker 2018). These hot outflows are often probed through X-ray observations, and their detections are often limited to starburst galaxies (D. K. Strickland & I. R. Stevens 2000; D. K. Strickland et al. 2004; N. Y. Yamasaki et al. 2009; A. Bogdan et al. 2013). Importantly, in these systems, significant cold ($T < 10^3$ K) outflows are also present (A. K. Leroy et al. 2015; J. Chisholm & S. Matsushita 2016; A. Fluetsch et al. 2019, 2021; E. Lopez-Rodriguez et al. 2021; E. Lopez-Rodriguez 2023). In smaller mass galaxies, hot outflows are mostly absent. When present, they are primarily attributed to active galactic nuclei (M. Mezcua et al. 2016). Instead, these galaxies frequently feature more moderate temperature winds, typically seen through an ionized component with low to moderate velocity, (possibly) non-escaping outflows (J. Chisholm et al. 2017; K. B. McQuinn, L. Zee & E. D. Skillman 2019; A. Concas et al. 2022; A. Marasco et al. 2023). These multiphase, metal-enriched galactic outflows also act as sources for the complex thermodynamical and chemical state of the CGM (e.g. J. Stern et al. 2016; J. K. Werk et al. 2016; A. Concas et al. 2022; B.-E. Choi et al. 2024; Y. Zheng et al. 2024).

Together, these processes result in a complex and evolving picture where galaxy formation simulations need to reproduce not just the observed galaxy properties but the thermal and chemical state of the baryon cycle that sets the properties of the CGM. The complexity and computational cost of large-scale cosmological simulations lead to shortcomings such as limited resolution, ineffective feedback, and inadequate modelling of some of the relevant physical processes (e.g. N. Katz 1992; Y. Dubois et al. 2014; M. Vogelsberger et al. 2014; J. Schaye et al. 2015; A. Pillepich et al. 2018; R. Davé et al. 2019). These are often alleviated through parametric calibration and/or sub-grid prescriptions for galactic winds, such as hydrodynamically decoupled wind particles (see M. Vogelsberger et al. 2020, for a review). Various galaxy outflow properties – the proportion of retained gas, entrained metals, distance of ejection – are either set or significantly affected by these modelling choices, with the mass–metallicity relation being a notable example (C. A. Tremonti et al. 2004; Y. M. Bahé et al. 2017; R. Davé et al. 2017; M. E. De Rossi et al. 2017; P. Torrey et al. 2019; Y. Dubois et al. 2021). Even in models featuring considerably higher resolution, some degree of artificial feedback enhancement is frequently required to reproduce the scaling relation between dark matter halo mass and stellar mass (J. Rosdahl et al. 2018; M. C. Smith et al. 2019; Y. Dubois et al. 2021; X. Shen et al. 2025). This often leads to single-phase, exclusively hot outflows from galaxy formation simulations that may be at odds with the observed multiphase winds (A. Concas et al. 2019; J. S. Bennett et al. 2025). Here, we investigate accounting for well-known non-thermal physics as a promising solution, focusing on three main components and their associated processes: magnetic fields, cosmic rays, and stellar ionizing radiation followed with full, on-the-fly radiative transfer.

Magnetic fields play a role in the baryon cycle even prior to the process of star formation, modifying the gas distribution across phases (C. C. Evirgen et al. 2019; B. Körtgen et al. 2019) and supporting molecular clouds against collapse, which drives higher star formation clustering (S. Martin-Alvarez et al. 2020; H. Robinson & J. Wadsley 2024). Magnetic fields also influence the star formation efficiency (C. Federrath & R. S. Klessen 2012; M. Zamora-Avilés et al. 2018), modify outflow gas dynamics, by, for example, affecting the mixing layer (A. Grønnow, T. Tepper-García & J. Bland-Hawthorn 2018; A. Shukurov et al. 2018; F. Van De Voort et al. 2021; J. Lee et al. 2025), and influence the CGM thermal instability (S. Ji, O. P. Oh & M. McCourt 2018). Magnetized outflows have been detected down to dwarf galaxy masses (S. Taziaux et al. 2025). This makes polarimetric observations of galaxy outflows a unique dynamical tracer, where the combination of radio and far-infrared observations enable studying large-scale and diffuse gas (radio) as well as small-scale and dense gas (far-infrared; A. S. Borlaff et al. 2023; E. Lopez-Rodriguez et al. 2023; S. Martin-Alvarez et al. 2024; D. Maglione et al. 2025). These observations allow probing the galaxy–halo interface in detail (M. Krause et al. 2020; E. Lopez-Rodriguez 2023), and reveal important kinematic information of outflows along the plane of the sky (Y. Stein et al. 2020; G. H. Heald et al. 2021; M. Stein et al. 2025).

Through its complex interactions with the surrounding medium, radiation is a pervasive contributor to the overall feedback landscape in galaxies: young, massive stars ionize their surroundings and pre-process gas through photoevaporation. This can lead to more efficient SN explosions (S. Geen et al. 2015; N. S. Sartorio et al. 2020). These effects also make radiation an important source of early stellar feedback, halting, and even suppressing ongoing star formation in molecular clouds depending on their mass (J. E. Dale, B. Ercolano &

I. A. Bonnell 2012; M. R. Krumholz et al. 2014; O. Agertz et al. 2020; S. H. Menon, C. Federrath & M. R. Krumholz 2023), and may even lead to the suppression of inflows on to the galaxy, leading to starvation of the smallest galaxies (H. Katz et al. 2020). Some studies show radiation is capable of directly driving winds from molecular clouds (S. H. Menon et al. 2023). Growing evidence, however, suggests that these small-scale effects may not lead to a stellar mass reduction in cosmological galaxy formation simulations. Instead, stellar radiation may lead to a minor star formation rate increase (S. Martin-Alvarez et al. 2023), as reduced star formation clustering decreases the mass-loading of galaxy outflows (J. Rosdahl et al. 2015; M. C. Smith et al. 2021).[1]

The potential of cosmic rays (CRs) as an effective pressure source further supporting galactic outflows has been long recognized (e.g. C. Pfrommer et al. 2007; M. Jubelgas et al. 2008; C. M. Booth et al. 2013; M. Salem & G. L. Bryan 2014; P. Girichidis et al. 2018; T. Buck et al. 2020; G. Dashyan & Y. Dubois 2020; P. F. Hopkins et al. 2021; M. Farcy et al. 2022; F. Rodríguez Montero et al. 2024; M. Farcy et al. 2025). This is due to their softer adiabatic index, lower energy losses away from dense ISM regions, and their ability to enhance SN momentum deposition even at small scales deep within the ISM (R. Diesing & D. Caprioli 2018; F. Rodríguez Montero et al. 2022). Numerical simulations have also found CRs capable of suppressing star formation in galaxies (M. Jubelgas et al. 2008; R. Pakmor et al. 2016; B. Commerçon, A. Marcowith & Y. Dubois 2019; P. F. Hopkins et al. 2020; A. Nuñez-Castiñeyra et al. 2022; C. M. Simpson et al. 2023; F. Rodríguez Montero et al. 2024). While CR propagation in galaxies is still not fully understood, and often simplifying assumptions are adopted to model their diffusion and streaming, and further improvements of their numerical modelling are required (L. Armillotta, E. C. Ostriker & Y.-F. Jiang 2021; P. Girichidis et al. 2022; P. F. Hopkins et al. 2022a, b; I. S. Butsky et al. 2023; T. Thomas, C. Pfrommer & R. Pakmor 2023; L. Armillotta et al. 2024; S. B. Ponnada et al. 2024), their distinct effects have established CRs as another fundamental player in the understanding of galaxy outflows and warrant further study.

The Pandora suite of high-resolution cosmological zoom-in simulations was introduced in Pandora I(S. Martin-Alvarez et al. 2023). That work employed the 17 zoom-in simulations in the suite to show that, in addition to the independent effects described above, the combination of stellar radiation, CRs, and magnetic fields leads to a complex interplay with pervasive effects across multiple galaxy properties (such as the stellar mass–halo mass relation, mass–size relation, kinematics, cusp–core halo profiles), and observables (such as optical appearance, resolved kinematics, galaxies colour–magnitude diagram, radio synchrotron emission). Pandora has also been employed to investigate how different combinations of non-thermal physics influence Ly α and Ly C escape and observables (Y. Yuan et al. 2024). Pandora serves as a pathfinder for our upcoming Azahar simulations (S. Martin-Alvarez et al. 2025; Martin-Alvarez et al., in preparation) featuring a larger cosmological volume of approx. $(10\,\mathrm{cMpc})^3$, and which have been already employed to study various high-redshift galaxy formation puzzles (e.g. C. Witten et al. 2024; T. Dome et al. 2025; Y. Yuan et al. 2025). In this work, we employ a subset of models from the Pandora suite, focusing on radiation and CRs to understand how the interplay of different non-thermal physics shapes star formation, galaxy outflow properties, and the resulting metal enrichment of the galaxy. The manuscript is structured as follows: Section 2 provides a brief introduction to the Pandora suite, with Section 2.2 summarizing the subset of models studied here. We report our main results in Section 3, investigating star formation and SN feedback (Section 3.2), outflow properties (Section 3.3), briefly comparing outflows with observations (Section 3.4), and concluding with an analysis of metal enrichment of the galaxy and enriched gas flows (Section 3.4.4). Our main conclusions are outlined in Section 4.

[1] See A. Emerick, G. L. Bryan & M.-M. Mac Low (2018) for the opposite effect, in low mass galaxies.

2 METHODS

2.1 The Pandora simulation suite

The galaxy formation simulations analysed in this work are a subset of the cosmological zoom-in Pandora suite (S. Martin-Alvarez et al. 2023). In this section, we summarize the basic characteristics of the RAMSES (R. Teyssier 2002) code used to generate the simulations, and the Pandora models studied.

The Pandora dwarf galaxy (halo virial mass $M_{\rm vir}(z=0) \sim 10^{10}\,\mathrm{M}_\odot$; with initial conditions introduced by M. C. Smith et al. (2019) under the label '*Dwarf1*' and re-generated for RAMSES) forms in a zoom-in sub-volume of 2.5 cMpc in width. In this region, the dark matter and stars collisionless particles have mass resolutions of $m_{\rm DM} = 1.5 \times 10^3\,\mathrm{M}_\odot$ and $m_* = 400\,\mathrm{M}_\odot$, respectively.

The adaptive grid is allowed to refine the zoom sub-volume down to a full-cell size of $\Delta x \sim 7$ physical pc. Cell refinement is triggered when the total mass of a resolution element, measured as $(\Omega_{\rm m}/\Omega_{\rm b})\, m_{\rm baryons} + m_{\rm DM}$, exceeds $8 \times m_{\rm DM}$. Here, $\Omega_{\rm m} = 0.3065$ and $\Omega_{\rm b} = 0.0483$ are the cosmological matter and cosmological baryonic matter densities, respectively. Refinement is also triggered when a resolution element fulfills the Jeans criterion $\Delta x > \lambda_J/4$. The Jeans criterion is disabled for cells with a comoving size $\Delta x > 1.8$ ckpc, to avoid excessive refinement in the low-density regions of the simulation. In this expression, λ_J is the local Jeans length.

Our magneto-hydrodynamics (MHD) models employ the RAMSES constrained transport (CT) solver by R. Teyssier, S. Fromang & E. Dormy (2006) and S. Fromang, P. Hennebelle & R. Teyssier (2006), and super-comoving coordinate implemented in S. Martin-Alvarez et al. (2018). This CT method numerically guarantees down to double precision the solenoidal constraint for the magnetic field ($\vec{\nabla} \cdot \vec{B} = 0$). Our radiative transfer (RT) models employ the RAMSES-RT implementation by J. Rosdahl et al. (2013) and J. Rosdahl & R. Teyssier (2015). The radiative flux budgets for each stellar particle are determined according to the age and metallicity-dependent spectral energy distributions of the BPASSv2.0 models (J. J. Eldridge, R. G. Izzard & C. A. Tout 2008; E. R. Stanway, J. J. Eldridge & G. D. Becker 2016). The overall RT configuration is similar to that of the SPHINX simulations (J. Rosdahl et al. 2018, 2022) that match well the reionization history of the Universe. The models with CRs employ the CR solver described by Y. Dubois & B. Commerçon (2016) and Y. Dubois et al. (2019), modelling CRs as an energy density representing ∼GeV protons. It accounts both for CR streaming (with streaming velocity equal to the Alfvén speed), anisotropic diffusion with a diffusion coefficient $\kappa_\parallel = 3 \times 10^{28}\,\mathrm{cm^2 s^{-1}}$ (M. Ackermann et al. 2012; A. C. Cummings et al. 2016; M. Salem, G. L. Bryan & L. Corlies 2016; C. Pfrommer et al. 2017b), and Coulomb and hadronic losses (F. Guo & S. P. Oh 2008). In the models studied here, magnetic fields and CRs are seeded by SN explosions, as described below. Further details of the RT, CR, and MHD implementations, and their employed configurations are provided in S. Martin-Alvarez et al. (2023).

Table 1. Subset of simulations studied in this work. From left to right, we indicate model symbol and label, whether the model includes magnetic fields (MHD), RT) and CRs, the stellar feedback configuration, and further details regarding the configuration of the simulation. From top to bottom, simulations account for additional baryonic physics. The full sample of Pandora models is provided in S. Martin-Alvarez et al. (2023).

	Simulation	MHD	RT	CR	Stellar feedback	Further details
	HD	✗	✗	✗	Mech	Standard hydrodynamical simulation
	HD + Boost	✗	✗	✗	Boosted Mech	Calibrated feedback through boosted SN: $2E_{\rm SN}$, $0.5M_{\rm SN}$.
	RTiMHD	✓	✓	✗	Radiation + Mag Mech	Including radiation and magnetic fields. SN inject $E_{\rm mag,SN}$.
	RTCRiMHD	✓	✓	✓	Radiation + CR Mag Mech	Pandora 'full physics' model; SN inject $E_{\rm mag,SN}$ + $E_{\rm CR,SN}$.

All Pandora models studied here employ our MTT (magneto-thermo-turbulent) star formation prescription (presented by T. Kimm et al. 2017; extended to MHD in S. Martin-Alvarez et al. 2020). In short, cells at the highest level of refinement (Y. Rasera & R. Teyssier 2006) are allowed to spawn new stellar particles when their gravitational pull is larger than the local MTT pressure support. They form stars according to the local MTT properties (P. Padoan & A. Nordlund 2011; C. Federrath & R. S. Klessen 2012) of the gas employing a Schmidt law (M. Schmidt 1959).

The models we study all include mechanical SN feedback (T. Kimm & R. Cen 2014; T. Kimm et al. 2015), which is injected into its hosting cell, and 48 (active) cell neighbours, according to an equal-solid-angle weighting. Each event injects (mass, momentum and energy) by selecting for each neighbour cell one out of two possible feedback modes: a momentum-conserving mode, injecting the SN terminal momentum, or an energy-conserving mode (Sedov), injecting the SN energy. Which solution is employed is determined by whether the ratio of swept-up versus ejected mass is above a given threshold (equation 7, T. Kimm et al. 2015). The SN-specific energy is $\varepsilon_{\rm SN} = E_{\rm SN}/M_{\rm SN}$, with $E_{\rm SN} = 10^{51}$ erg and $M_{\rm SN} = 10$ M$_\odot$ – except for HD + Boost, which features $\varepsilon_{\rm SN,\,Boost} = 4\,\varepsilon_{\rm SN}$. In the studied models including MHD, these explosions inject 1 per cent of their energy into the magnetic component ($\gtrsim 10^{-5}$ G when injected at scales of ∼10 pc; reproducing the magnetization observed at the scale of SN remnants; E. Parizot et al. 2006) through two small-scale toroids with arbitrary orientations. This implementation reproduces magnetic fields in observed galaxies (S. Martin-Alvarez et al. 2021, 2024; T. Dacunha et al. 2025). Additional details of this implementation are provided in appendix A of S. Martin-Alvarez et al. (2021). Similarly, in the studied model including CRs, 10 per cent of the SN energy (extracted from its mechanical energy budget) is injected into the CR energy, motivated by observations (G. Morlino & D. Caprioli 2012; E. A. Helder et al. 2013), and is a standard value employed by similar studies (e.g. C. Pfrommer et al. 2017a; I. S. Butsky & T. R. Quinn 2018; F. Rodríguez Montero et al. 2024).

2.2 A representative subset of models

In this work, we restrict our analysis to a subset of the Pandora simulations. The subset has been selected to provide a representative view of the main physical effects at play in the interplay between star formation and galaxy outflows. The four selected models are summarized in Table 1, and correspond to: (i) the standard hydrodynamics model characteristic of traditional simulations (HD), (ii) an 'enhanced' SN feedback representative of calibrated hydrodynamical models (HD + Boost; with SN specific energy increased by 4×), (iii) a model including the important ISM non-thermal physics of radiation and magnetic fields (RTiMHD), and (iv) the Pandora full-physics simulation incorporating CRs as well (RTCRiMHD). These are the models highlighted as models of interest by S. Martin-Alvarez et al. (2023).

To identify the galaxy of interest in the simulation, we select its host halo at $z = 8$, and determine its exact position through a shrinking spheres algorithm (C. Power et al. 2003). We determine its position in subsequent snapshots (both forward and backward in time) by selecting the innermost 500 particles and finding their updated centre-of-mass, followed by the recursive application of our shrinking spheres method. For each snapshot, each galaxy is associated with its hosting halo, extracted from a halo catalogue generated using HALOMAKER (D. Tweed et al. 2009). When multiple progenitors are identified, we only employ the most massive one for our analysis here. This method, and its on-the-fly application to RAMSES cosmological simulations will be further detailed in Martin-Alvarez et al. (in preparation+). The main galaxy measurements are performed in the central region of the halo ($r < 0.2\,r_{\rm halo}$, with $r_{\rm halo}$ the virial radius of the halo), as described in the corresponding measurement descriptions provided in Section 3.

3 RESULTS

3.1 A qualitative picture of SN-driven outflows accounting for different physical processes

Fig. 1 provides a qualitative comparison of the four different Pandora dwarf galaxy simulation models, illustrating the impact of varying physical processes on SN-driven outflows. Each panel is 5 kpc across, approximately encompassing the central galactic region ($0.2\,r_{\rm halo}$, with $r_{\rm halo}$ the virial radius of the dark matter halo). The columns, from left to right, correspond to the main models we study here: standard hydrodynamics (HD), calibrated SN feedback hydrodynamics (HD + Boost), RT and MHD (RTiMHD), and our 'full-physics' simulation incorporating radiation, CRs, and MHD (RTCRiMHD). In the top row, we show the gas (blue) and stellar (gold) mass-weighted mean densities. The second row of the figure displays the gas temperature. The third row shows gas density flows, separated according to the radial velocity of each cell ($v_{\rm r}$) into inflows (blue) and outflows (gold and red), with the full gas density field displayed in greyscale for context. Gas is selected as inflowing ($v_{\rm r} < -v_{\rm vir}$) or outflowing ($v_{\rm r} > v_{\rm vir}$ as gold tones; $v_{\rm r} > 40$ km s^{-1} further coloured in red), where $v_{\rm vir} \sim 12.5$ km s^{-1} is the virial velocity of the halo. Panels in the bottom row display the mass-weighted metallicity in solar units ($Z_\odot = 0.012$; R. Schneider et al. 2012). We include isocontour lines to guide the eye to the location of the main galaxy and satellites. To avoid spurious variations of metallicity measurements in regions of undersampled (or extremely low) stellar mass, we set the map to null values outside the outermost contour (i.e. for stellar surface densities lower than 10^5 M$_\odot$ kpc^{-2}).

The distribution of gas around the galaxy varies notably across our models. In the HD model, we observe relatively large and hot outflow bubbles (∼1–2 kpc) confined by dense gas shells with

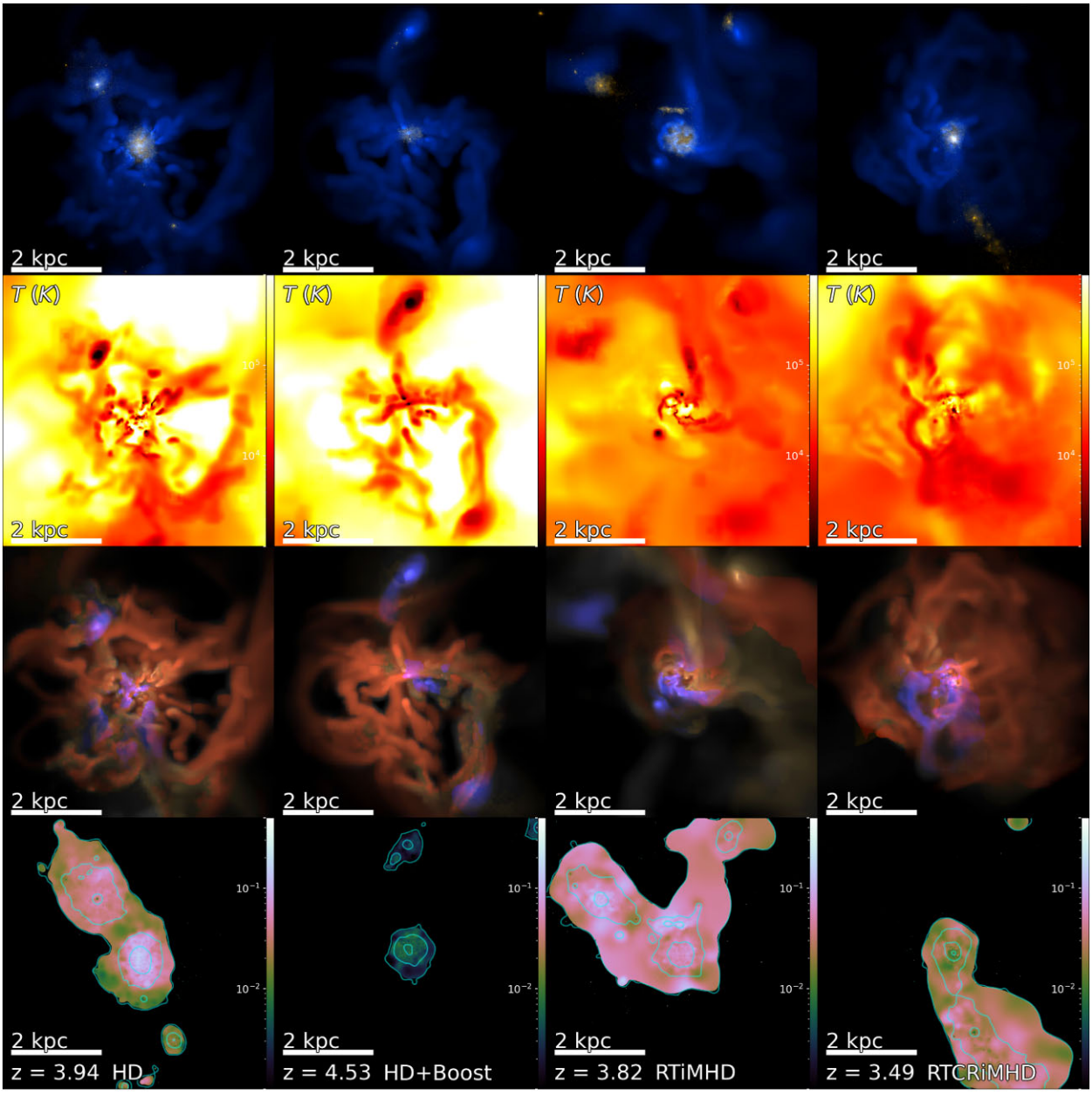

Figure 1. Projected views centred on the Pandora dwarf illustrating outflow events across our four studied models. The area displayed in each panel approximately encompasses the central galactic region ($0.2\,r_{\rm halo}$), 5 kpc across. Each of the columns, from left to right, corresponds to the following models: standard HD, HD + Boost, RTiMHD, and our 'full-physics' simulation with radiation, CRs and MHD (RTCRiMHD). Top row panels: Mass-weighted densities for the gas (blue) and stellar (gold) components. Second row panels: Gas temperature maps. Third row panels: Gas density flows separated according to radial velocity ($v_{\rm r}$) into inflows (blue; $v_{\rm r} < -v_{\rm vir} = 12.5$ km s^{-1}) and outflows (golden; $v_{\rm r} > v_{\rm vir}$, and red for faster outflows $v_{\rm r} > 40$ km s^{-1}). For further visual guidance, in this row we display the full gas density field using a grey scale. Bottom row panels: Mass-weighted stellar metallicity. To guide the eye, the overlaid contours display the $[10^5, 10^6, 10^7, 10^8]$ M$_\odot$ kpc^{-2} stellar surface density isocontours. Galactic outflows in HD and HD + Boost appear hotter and with rugged and defined shock structures. Including radiation reduces the outflows, whereas CRs lead to temperate and more homogeneous outflows, as well as complex metallicity topology.

irregular and turbulent surfaces. These bubbles contain the bulk of the outflowing gas mass. The properties of outflow bubbles are even more pronounced in the HD + Boost case, with bubbles that reach higher temperatures and larger sizes, despite a lower star formation rate (SFR). The bubbles exhibit a complex substructure, resembling multiple bursts of SN-driven winds that are carving multiple holes in the CGM. Conversely, the high temperature bubbles in the RTiMHD model do not extend significantly beyond the galaxy (e.g. third panel of the RTiMHD column, seen as outflowing, high-density regions), and due to the presence of the radiation field the gas surrounding the galaxy has a smooth appearance. The significantly more diffuse stellar component in this model (top panel; see also fig. 4 in S. Martin-Alvarez et al. 2023) leads to a lower clustering of stellar feedback, discussed further in Section 3.2. The RTCRiMHD model

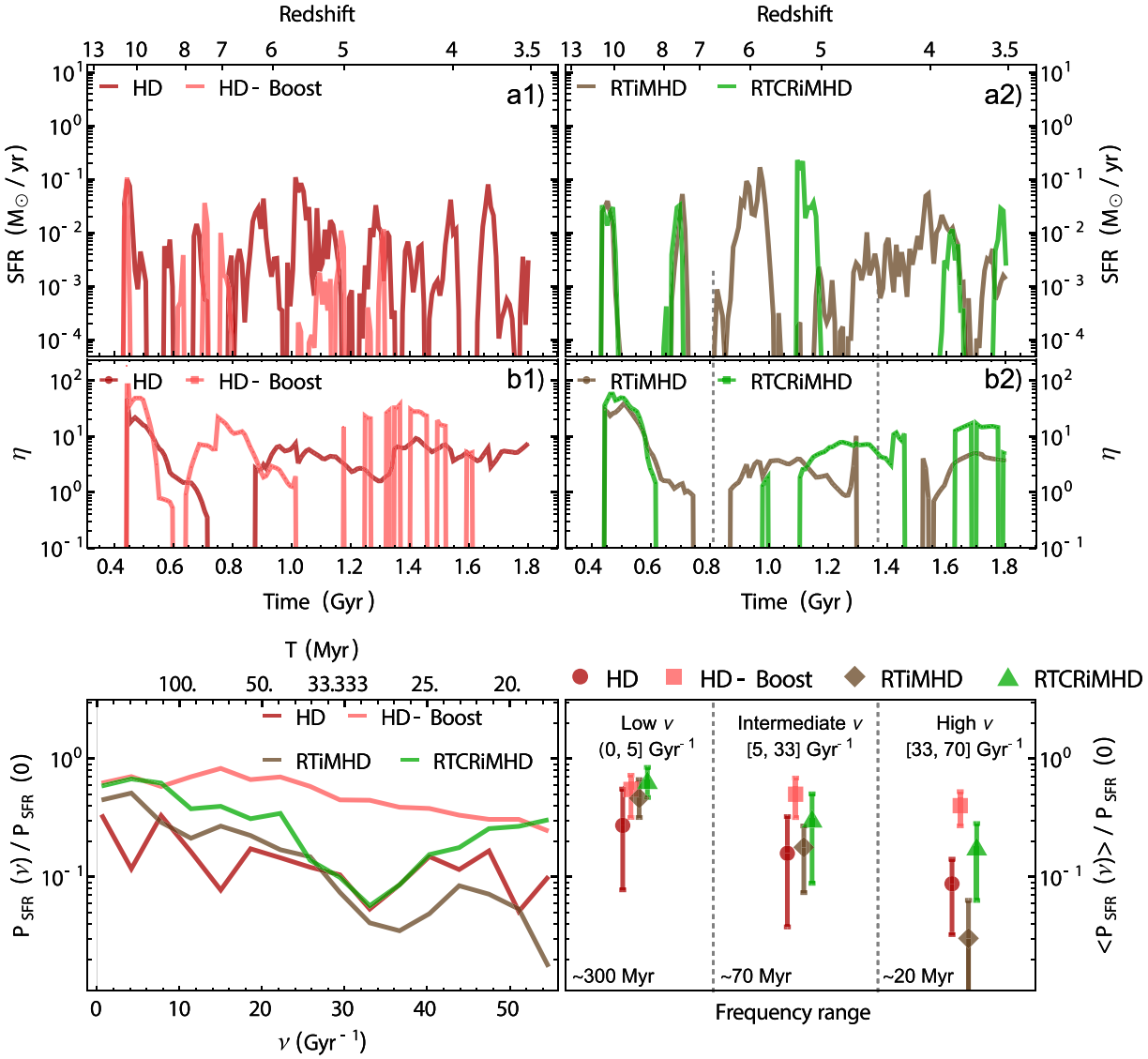

Figure 2. Top row: SFR for our hydrodynamical models HD and HD + Boost (panel a1), and for our more complex models including stellar radiation and magnetic fields RTiMHD, as well as CRs, RTCRiMHD (panel a2). Central row: Outflowing gas mass-loading factor ($\eta = \dot{M}_{\rm gas}/{\rm SFR}$; see text for further details) radially ejected through a spherical shell positioned at $0.5\,r_{\rm halo}$. Including radiation leads to a more continuous SFR, whereas its combination with CRs leads to a more bursty star formation history. The calibrated feedback HD + Boost and full physics RTCRiMHD simulations attain the highest outflow mass-loading factors. The RTiMHD has the lowest η values, albeit those remain comparable to the HD scenario. Bottom row: Fourier transform of the star formation history for the same models, normalized to the zero-frequency mode (left panel). The average power is separated into the three frequency regimes corresponding to long, intermediate, and short time-scales (right panel).

shows outflowing bubbles comparable in size to those in the HD model, but with smoother surfaces due to the presence of the non-thermal components. This RTCRiMHD model also has a temperate and outflowing diffuse envelope surrounding the galaxy, suggesting a scenario where outflows are initially driven by SNe and subsequently expelled further by cosmic ray pressure in a more isotropic fashion. Interestingly, stellar metallicity distribution is very sensitive to the different physics models, with the dwarf galaxy in the HD + Boost simulation being extremely metal poor (see further Section 3.4), while in the RTCRiMHD simulation dwarf and its surroundings are enriched to $Z_* \sim 0.1\,Z_\odot$, and exhibit complex metal distribution and gradients.

3.2 Bursty and concentrated star formation drives mass-loaded outflows

Before we proceed to qualitatively characterize the properties of galaxy outflows across our different models, we investigate the interrelation between the star formation histories (SFHs) and the galactic outflows in the Pandora simulation suite. To this effect, we show in Fig. 2 the SFR and outflowing gas mass-loading factors ($\eta = \dot{M}_{\rm gas}/{\rm SFR}$) across different simulation models. The top row shows the SFR for our hydrodynamical models (panel a1), and for the more complex models including stellar radiation and magnetic fields (panel a2), both with and without CRs. The bottom row presents the

outflowing gas mass-loading factor η through a spherical shell with a thickness of 200 pc positioned at $0.5\,r_{\rm halo}$.[2]

The onset of significant star formation is comparable across all models, and occurs at ~ 0.4 Gyr. The models with stellar radiation have a somewhat lower initial SFR (up to 0.03 $M_\odot$ yr^{-1} instead of 0.1 $M_\odot$ yr^{-1}), as the stellar radiation acts as a source of early stellar feedback. This initial star formation event continues for $\sim$100 Myr in the HD model, whereas it is rapidly halted by the 'boosted' SN feedback in the HD + Boost model, and by stellar radiation and SNe in the RTiMHD and RTCRiMHD models. After a second star formation event at $t \sim 0.7$ Gyr, the evolution of the models starts to differ more significantly. We focus on our hydrodynamical models first (panel a1). Despite its rapid variation on time-scales of $\lesssim 50$ Myr (frequencies of $f_{\rm SFR} \sim (50\,{\rm Myr})^{-1}$), the HD model maintains an approximately continuous SFR. The HD + Boost model exhibits a notably different SFH, characterized by an 'on' and 'off' SFR. Its star formation proceeds through three main extended bursts of star formation, with a typical duration of $\lesssim$ 200–300 Myr. The RTiMHD model (panel a2) shows a 'flatter' and uninterrupted star formation during the $z = 7$ to $z = 6$ and $z = 5$ to $z = 4$ periods. Its star formation resembles that of the HD model, but with much weaker short-time-scale fluctuations. The RTCRiMHD model has a particularly episodic SFH, with sharp bursts of star formation separated by extended quiescent periods. Its episodes of star formation differ from the HD + Boost case by being more cyclic and concentrated in time. To quantify these variations in further detail, the bottom left panel of Fig. 2 shows the Fourier transform of each SFH, normalized by their corresponding 0th mode (proportional to the total stellar mass) to account for the differing stellar masses at the end of the studied period. We identify three main regimes of interest in the frequencies of SFR fluctuations: long time-scales of $\sim$300 Myr, intermediate time-scales of $\sim$70 Myr, and short time-scales of approximately $\lesssim 20$ Myr. The average power in each regime is shown in the bottom right panel of the same figure. The Fourier transform of the star formation history confirms a more episodic SFH for the RTCRiMHD model that rapidly transitions from quiescent to star forming, and the role of radiative transfer (especially notable in RTiMHD) in smoothing out the star formation variability on short time-scales. The observed behaviour of the RTCRiMHD model is attributed primarily to the combined effect of the non-thermal pressures from CRs and magnetic fields. Their pressure support allows gas clouds to grow in mass until they become supercritical, leading to their rapid collapse and concentrated star formation. We note that this effect is likely sensitive to the value of $\kappa_\parallel$ employed – e.g. B. Commerçon et al. (2019) and G. Dashyan & Y. Dubois (2020) attain higher ISM gas densities for higher $\kappa_\parallel$, potentially leading to increased burstiness.

As expected, these variations in the overall shape and properties of the SFHs across our models have important effects on the mass-loading factors measured for our dwarf galaxy. The HD simulation has approximately sustained outflows, with low mass-loading factors ranging around $\sim$ 1–5. The HD + Boost model reaches the highest mass-loading factors we measure despite its low SFR (and its lack of concentrated SN events), due to the enhanced energy deposition per SN in this model. The RTiMHD model has the lowest mass-loading factors, and during its multiple periods of low or no star formation, the mass-loading tends to $\eta \to 0$. The RTCRiMHD simulation has also high mass-loading factors, of the order of $\sim$10, and comparable to the HD + Boost model. Notably, these values are reached with significantly lower energy injection, underscoring the efficiency of its episodic star formation and CR-driven outflows. The different properties associated with the outflows emerging from each model are discussed in Section 3.3.

The correlation between star formation and subsequent outflows is driven by SN events, with their effectiveness influenced by their small-scale ISM environments, which will also affect the gas phases entrained in galaxy outflows. We show the thermodynamical properties of the gas cells where SN events take place in Fig. 3. Panels display the probability density functions (PDFs) for all the SNe events in each simulation (from $z = 8$ to $z = 3.3$), both for the hosting cells gas density (top panel) and temperature (bottom panel).

Overall, the gas density distribution of cells hosting SN events is bimodal, with a dominant peak at low densities of $\sim 10^{-27}$ g cm^{-3}–10^{-26} g cm^{-3}, and a secondary peak at high densities of $\sim 10^{-21}$ g cm^{-3}. This bimodal distribution is physically driven: stars are formed in dense regions where, in the absence of any feedback process, they explode as SNe with some delay after their formation. This occurs inside or in the vicinity of dense clouds with $\rho_{\rm gas} \gtrsim 10^{-22}$ g cm^{-3}. Subsequent SN events originating from the same localized star formation event will typically occur within and around the sites of prior SNe events, which are very hot ($T \approx 10^7$–10^8 K), leading to a tail towards lower densities as supernova remnants expand, and ultimately leading to a peak at densities of $\sim 10^{-27}$ g cm^{-3}. Notably, it is precisely within these lower density, higher temperature gas where SNe feedback becomes most effective (T. Naab & J. P. Ostriker 2017; F. Rodríguez Montero et al. 2022). While T. Kimm & R. Cen (2014) have demonstrated that our mechanical prescription alleviates overcooling and recovers the expected momentum injection (K. Thornton et al. 1998), there are additional numerical considerations to note in a realistically simulated ISM. For example, D. Martizzi et al. (2015) and C. G. Kim & E. C. Ostriker (2015) have shown that the presence of ISM inhomogeneities does not significantly affect the terminal momentum injected by SNe, hence supporting the use of momentum-injecting solutions in galaxy formation modelling (P. F. Hopkins et al. 2018; M. C. Smith et al. 2018; I. Shimizu et al. 2019). C. G. Kim & E. C. Ostriker (2015) have also studied shocks propagation, showing that they reach further distances along low density channels. The vast majority of SN events in our simulations take place at $\Delta x < 10$ pc ($\sim$90 per cent; and 80 per cent for HD + Boost), with virtually all the remaining events taking place at $\Delta x < 15$ pc and low gas densities $\rho_{\rm gas} < 10^{-24}$ g cm^{-3}. We estimate $\gtrsim 80$ per cent of events use our adiabatic mode. Note that these ratios, derived from central host cells, may slightly underestimate the proportion of snowplow events; although this is alleviated by the simulation code requirement for contiguous cells not being more than one level lower resolution, and our refinement strategy of resolving the local Jeans length with at least 4 cells. For SNe in dense media, a higher preservation of terminal momentum at the end of the snowplow phase is expected for higher resolutions, with E. S. Gentry, P. Madau & M. R. Krumholz (2020) estimating an increase of 1.4× if our models featured resolutions of 1 pc.

[2]Due to the rapid variability of star formation in dwarf galaxies, to compute the η values we smooth the star formation rate. Here, we assume a $\sigma \sim 0.042$ Gyr (corresponding to FWHM of $\sim$100 Myr), further including a 10^{-4} $M_\odot$ yr^{-1} floor to avoid artificially large η during periods of negligible SFR. To consider gas outflowing, we require a cell to have a positive radial velocity $v_{\rm r} > v_{\rm vir}$, which reduces spurious contributions to galaxy outflows. We also include a uniform $\Delta t = 0.2$ Gyr delay for the $\eta\,(0.5\,r_{\rm halo})$ calculations, which corresponds to a local maximum in the cross-correlation of SFR and outflows, and is equal to the approximate time for a gas outflow to travel from the galaxy centre to $0.5\,r_{\rm halo}$ at $\sim 2\,v_{\rm vir}$ – approximately our measured mass-weighted average velocity of outflows.

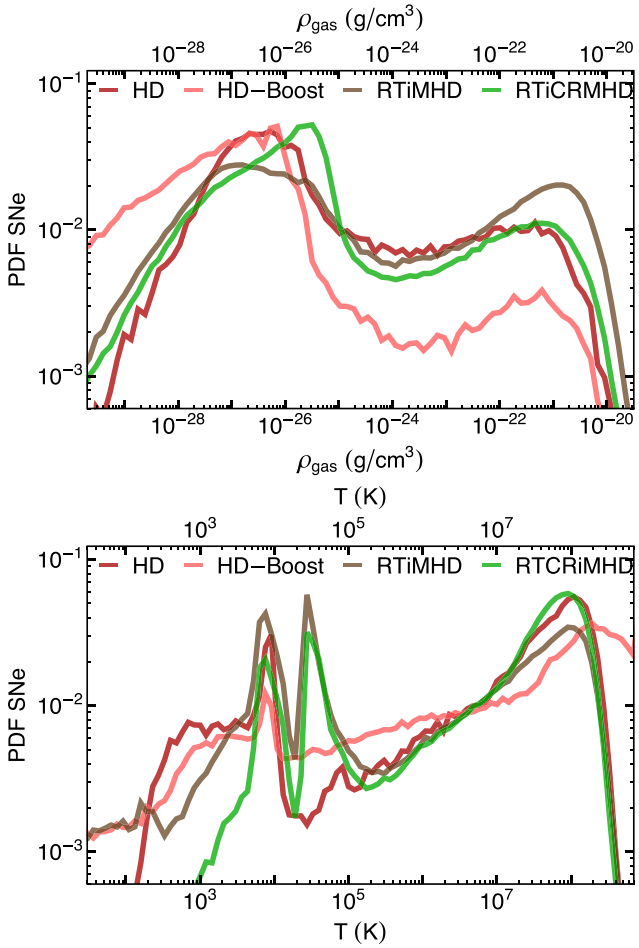

Figure 3. PDF of the small-scale environmental thermodynamical properties where SN events take place in each of the models: gas density (top panel) and gas temperature (bottom panel). Across all simulations, most SNe take place at densities $\rho \sim 10^{-26}$ g cm^{-3}. Different galaxy formation physics leads to notably different fractions of SN events taking place at high densities ($\rho > 10^{-24}$ g cm^{-3}). Early feedback in the form of stellar radiation significantly increases the number of SNe at high densities by reducing star formation (and consequently SN) clustering, whereas 'boosted' SN feedback leads to their drastic reduction, due to effectiveness of few events in dispersing dense gas. The RTCRiMHD simulation shows the strongest temporal SN clustering, while maintaining the proportion of events taking place in dense, photoheated regions.

In the HD model, most SN events occur at the low gas density peak, with a relatively flat distribution from intermediate densities of $\rho_{gas} \sim 10^{-24}$ g cm^{-3} to 10^{-21} g cm^{-3}, and virtually no events taking place at higher densities. The HD + Boost model significantly suppresses the number of SN events at densities $\gtrsim 10^{-25}$ g cm^{-3} (approximately 5× less frequent than in the HD simulation). Such suppression of low-effectiveness and rapidly cooling environments, combined with a higher energy deposition per SN (4× higher than the canonical value), leads to much more effective feedback in the HD+Boost simulation. Additionally, the tail of SNe taking place at the lowest densities is much flatter, with HD + Boost being the only model featuring a significant number of SN events in the $\rho_{gas} \lesssim 10^{-28}$ g cm^{-3} regime, resulting from the higher energy deposition effectively inflating larger bubbles and clearing the gas to lower densities. The above described density PDFs translate almost directly to the temperature PDFs of the HD and HD + Boost models, where the low gas density peak directly corresponds to high temperature environments pre-processed by previous SNe ($T \sim 10^7 - 10^8$ K) and the high density events take place in the thermally stable warm ionized medium with $T \sim 10^4$ K, or inside colder star-forming regions with $T \lesssim 10^3$ K. Incorporating stellar radiation in the RTiMHD model results in the lower concentration of star formation, and a subsequent reduction of both temporal and spatial SN clustering. Although radiation locally reduces the gas density prior to the occurrence of the first SN events (S. Walch & T. Naab 2015), the reduced clustering we measure is consistent with the observed increase of SNe events at high gas densities. Radiation provides an effective early feedback that halts ongoing star formation in large gas clouds, photo-heating them to 3×10^4 K. In the RTiMHD simulation, the increased proportion of SN events at high densities predominantly take place at this photoheating temperature of $T \sim 3 \times 10^4$ K (M. Y. Grudić et al. 2022), which will have implications for the properties of the gas entrained in outflows. Finally, the combination of stellar radiation with CRs in the RTCRiMHD model leads to a gas density PDF of SNe host cell which is comparable to that in the HD simulation. Once again, a higher temporal clustering of star formation, and the subsequent SNe drive an increase of the proportion of explosions taking place at lower densities and high temperatures, while maintaining a large proportion of events taking place in dense, photoheated regions. Furthermore, the inclusion of CRs leads to a slight increase of (diffuse) ISM densities in the presence of additional non-thermal pressure terms (G. Dashyan & Y. Dubois 2020), and the low density peak of SN events is displaced to slightly higher densities of $10^{-26} - 10^{-25}$ g cm^{-3} instead of slightly below.

The reduction of SN feedback efficiency through the inclusion of radiation in our simulations is well-explained by the distribution of SN events across the different ISM phases and environments combined with a steady star formation. We also find large variations of the SNe host cell PDFs for our 'boosted' SN feedback model, but its increased efficiency is most likely the result of a considerably higher energy deposition per SN event, with the lower number of events at higher densities being secondary. While our 'full-physics' model has some observable variations in the SNe host cell PDFs, the episodic star formation and the properties of the outflowing gas are the main culprits for its higher outflow efficiency. We will investigate the physical properties of such outflowing gas in the next section.

3.3 Dense and temperate CR-driven galactic outflows

To review how outflow-related quantities and their pressure contributions are distributed around the Pandora dwarf galaxy, we show radial profiles representative of star formation episodes at $z = 3.5$ in Fig. 4. The top row of panels show the pressure profiles for different physical components: thermal (solid), magnetic (dotted), radiative (dotted–dashed), and cosmic ray (dashed), whenever included. We provide further details on their computation in Appendix A. To illustrate how representative these pressure profiles are, and study their variability in high-versus-low SFR regimes, we discuss time-aggregated radial pressure profiles in Appendix B. The central row shows the fractional contribution to the total pressures for each of the pressure components shown in the top panels. The bottom row of panels display the density profiles, with solid lines representing the total density and dotted lines indicating the outflowing gas. The radial profile of the net outflowing momentum is overlaid with golden solid lines, and shown as dashed curve at radii where the net momentum is inflowing. Vertical lines in all panels mark radii of interest: a proxy for

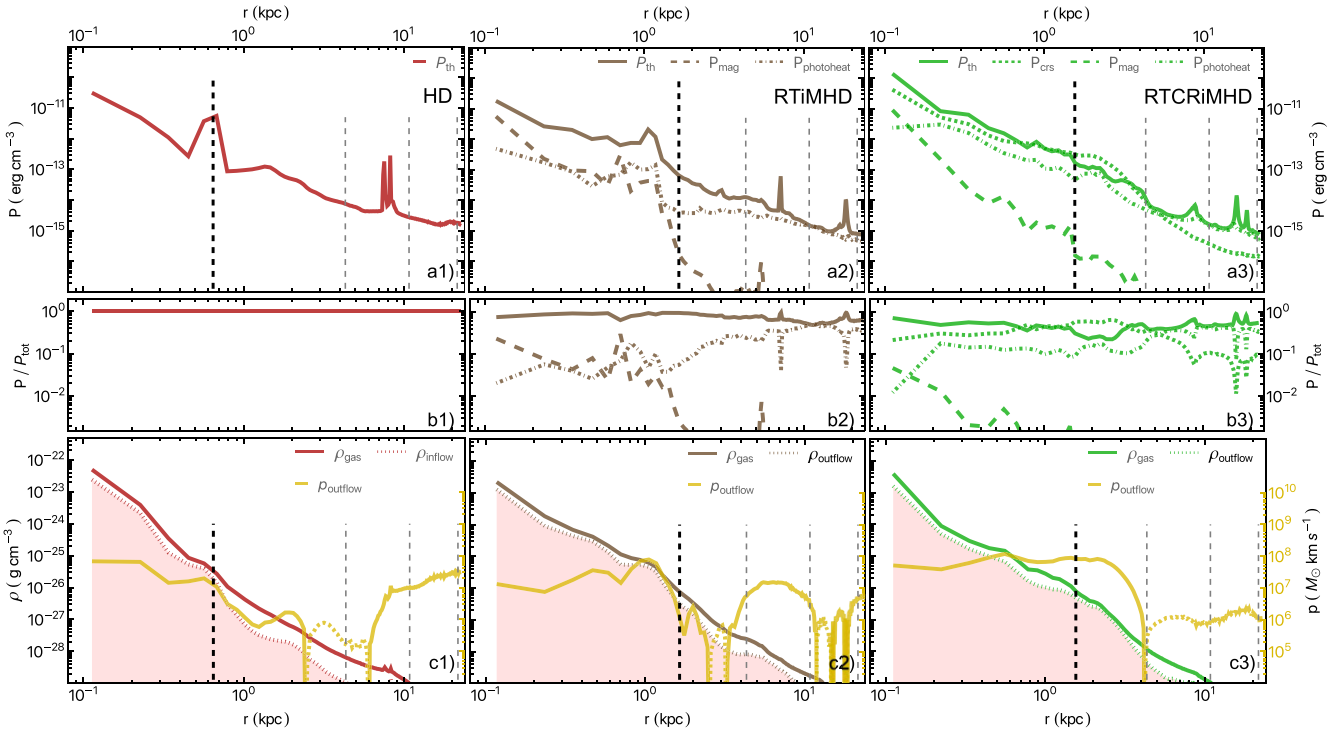

Figure 4. Radial profiles for various outflow-related quantities, centred on the Pandora dwarf. Profiles correspond to star formation episodes at $z = 3.5$, and are representative of times with non-negligible star formation (Appendix B). The RTCRiMHD model in particular exhibits larger variations due to its burstier star formation. Top row: Pressure profiles for the thermal (solid), magnetic (dotted), radiative (dotted–dashed), and cosmic ray (dashed) components. **Central row**: Fractional pressures for the same components as shown in the top row. Bottom row: Density profiles, separated into total (solid line) and outflowing components (dotted line). We overlay the radial profile of the net outflowing momentum using golden solid lines, displayed as dashed for radii when the net momentum is inflowing. We include additional vertical lines in each panel corresponding to twice the half-mass radii of the stellar component (thick black dashed line, $2\,r_*$), and the 0.2, 0.5, and 1.0 $r_{\rm halo}$ (grey dashed lines). In the models without CRs, outflowing gas (e.g. $\sim$ 1 kpc in panel b2) is thermally supported (panels a1 and a2). Conversely, outflows in the RTCRiMHD model ($\sim$ 3 kpc in panel b3) are dominated by CR pressure (panel a3). Overall, in the RTCRiMHD simulation, thermal pressure dominates across most radii – although with important contributions from the other pressure components. CRs dominate in the outflow bubbles and provide significant support at $r \lesssim 3\,r_*$. Magnetic pressure is only globally important inside the galaxy, whereas the radiative photoheating pressure becomes more important at large radii, driving the thermal pressure through photoheating.

the size of the galaxy at twice the stellar half-mass radius (thick black dashed line) and the 0.2, 0.5, and 1.0 fractions of $r_{\rm halo}$ (grey dashed lines).

The pressure profiles in the top row provide useful insights into the mechanisms supporting gas at different galactocentric distances, and serve as proxies for the pressure gradients that drive outflows (see e.g. F. Rodríguez Montero et al. 2024). The thermal pressure profiles approximately follow power laws (roughly following $\propto r^{-2}$) up to $\sim 0.5\,r_{\rm halo}$, with distinct, sharp peaks attributable to substructures. Overall, thermal pressures are comparable between the HD and RTiMHD models, while the RTCRiMHD simulation has a higher thermal pressure especially in the central region. Across all models, the thermal component dominates the pressure budget at all radii $r > 0.1$ kpc, except some narrow spatial regions where $P_{\rm CR}$ dominates. When reviewing other pressure components through their fractional contribution (middle row), magnetic pressure only dominates locally in high density regions of the ISM. This suggests that magnetic fields do not directly affect outflowing gas support, and intervene primarily through their contribution to star formation regulation. The photoheating pressure dominates the contribution from stellar radiation. We find this pressure only dominates the local pressure in the regions where massive stars from recent star formation events are located. However, at larger radii outside the galaxy it is comparable to the thermal pressure, and is responsible for increasing the thermal pressure through its heating effects, featuring a higher energy budget.[3] Interestingly, in our RTCRiMHD simulation, the photoheating and CR pressures are comparable up to $\sim 0.2\,r_{\rm halo}$, and moderately dominated by the CRs. The CR pressure is in fact the second most significant pressure source within $r < 0.2\,r_{\rm halo}$. The CR pressure also dominates in gas outflow fronts, particularly evident at $r \sim 3$–4 kpc which correlates with the edge of the $p_{\rm outflow}$ and outflowing gas density (panel c3). Beyond this radius, the CR pressure drops back to the underlying pressure profile. When the pressure profile is computed without the contribution from the outflowing gas the higher pressure of CRs at $r \sim 3$ kpc is not present, and the non-outflowing CR pressure profile scales as an approximate power-law out to the edge of the dark matter halo ($r \in [1, 15]$ kpc). The bottom panels of Fig. 4 provide further information about the relationship between the pressure profiles and gas outflows. The galactic outflows in the HD simulation, reflected by peaks in both density and momentum, show relatively unchanged pressures. The only exception is the SN-triggered pressure peak at $r \sim 0.6$ kpc accelerating a new outflow. In contrast, the RTCRiMHD outflows are characterized by concentrations of CR pressure, which

[3] Note that at pressure equality, relativistic fluid energies such as the radiative one have a higher energy budget ($u_{\rm rad} = 3\,P_{\rm rad} = 3\,P_{\rm CR}$), whereas the thermal ($u_{\rm th} = \frac{3}{2}\,P_{\rm th}$) and magnetic ($u_{\rm mag} = P_{\rm mag}$) components have a P/u ratio closer to unity.

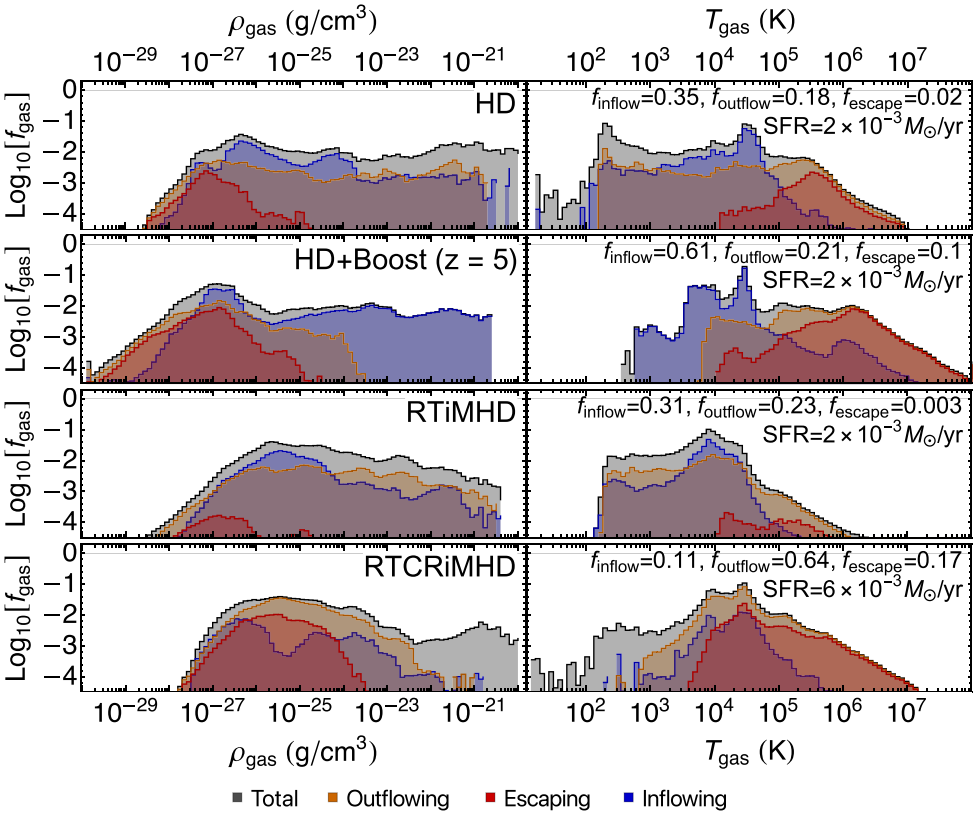

Figure 5. Gas mass fraction distribution functions as a function of gas density (left column) and gas temperature (right column) for the central galactic region ($r < 0.2\,r_{halo}$). Distributions are shown for snapshots of non-negligible star formation activity in the galaxy, at $z = 3.5$ (except for HD + Boost, see main text). Total gas fraction (grey histograms), inflowing gas fraction (blue histograms, $v_{gas,radial} < v_{vir} \sim 12.5$ km s^{-1}), outflowing gas fraction (orange histograms, $v_{gas,radial} > v_{vir}$) and escaping gas fraction (red histogram, $v_{gas,radial} > v_{esc}(r = 0.2\,r_{halo})$) are shown for our four simulation models (top to bottom rows). Each temperature panel lists the SFR of each galaxy during the past 100 Myr, and the total mass fraction of the inflowing, outflowing and escaping gas component. The RTCRiMHD simulation has lower inflow rates as well as higher outflow and escaping rates per given SFR. The outflowing gas is also colder and denser, particularly notable in the escaping gas regime.

decreases sharply beyond the outflowing momentum shells (e.g. $r \sim 2$ kpc), in agreement with outflow-injected CRs in the halo and CGM. By providing additional support against the pull from the gravitational potential, both the photoheating and CRs pressures will promote denser outflows that will reach larger distances from the galaxy. This is reflected in higher net outflowing momenta at $r \lesssim 1$ kpc in these two models ($p_{outflow} \sim 10^7$ M$_\odot$ km s^{-1} for RTiMHD; $p_{outflow} \sim 10^8$ M$_\odot$ km s^{-1} for RTCRiMHD) when compared with HD ($p_{outflow} \sim 10^6 - 10^7$ M$_\odot$ km s^{-1}). These pressure distributions and their properties are broadly preserved during episodes of non-negligible star formation, but vary at times of quiescence (sSFR < 1 Gyr^{-1}), especially for models with burstier star formation (Appendix B).

To review the physical properties of galaxy outflows in the context of the multiphase ISM, we show in Fig. 5 the distribution of mass within the central galactic region ($r < 0.2\,r_{halo}$) at times of non-negligible star formation. Gas mass is separated according to the flow properties. The panels show the gas mass fraction distribution as a function of gas density (left column) and gas temperature (right column). The grey histograms depict the overall gas mass fraction distribution for each simulation, and additional coloured histograms show the mass fractions of inflowing (blue histograms, $v_{gas,radial} < -v_{vir} \sim -12.5$ km s^{-1} to exclude gas with relatively low velocities), outflowing (orange histograms, $v_{gas,radial} > v_{vir}$), and escaping (red histograms). Escaping gas is selected according to $v_{gas,radial} > v_{esc}(r = 0.2\,r_{halo})$, with escape velocities $v_{esc} \sim 33-37$ km s^{-1}. Note that the mass of outflowing gas is a fraction of the total mass, and the mass of escaping gas is a fraction of the mass of outflowing gas. From top to bottom, panels correspond to the HD, HD + Boost, RTiMHD, and RTCRiMHD simulations at $z \sim 3.5$ (except for HD + Boost[4], shown during its star formation event at $z = 5$), but selected to be representative of the dwarf galaxy across times when its SFR $\neq 0$. Additional integrated information about the current state of the galaxy is provided in the top right corner of the temperature panels: the SFR of each galaxy over the past 100 Myr, and the integrated fraction of gas mass in different outflowing phases.

We focus first on the left-hand panels, where gas densities typically range from $\rho_{gas} \sim 10^{-28}$ to $\sim 10^{-20}$ g cm^{-3}. In HD and HD + Boost the mass fraction PDF is approximately uniform over all gas densities, with a moderate peak around $\rho_{gas} \sim 10^{-27} - 10^{-26}$ g cm^{-3}. Including radiative transfer in our RTiMHD model leads to further gas accumulation in the diffuse gas phase with $\rho_{gas} \sim 10^{-26} - 10^{-24}$ g cm^{-3}, and a reduced proportion of gas at

[4]Due to lack of significant star formation past $z \sim 5$ in HD + Boost, at $z = 3.5$ the model does not have any prominent outflows. This is primarily due to the absence of any significant SN feedback for a prolonged time (O. Agertz, R. Teyssier & B. Moore 2009). Therefore, we opt to present its PDF during the star formation event at $z = 5$, when it features an SFR comparable to the other models at $z = 3.5$.

higher densities. The PDF in the 'full-physics' RTCRiMHD model exhibits the same behaviour as in the model including radiation but has a cut-off at low densities instead of the long tail seen for HD, HD + Boost and RTiMHD. As shown by the red histograms, this tail towards lower densities is dominated by escaping gas, which typically exhibits an approximately log-normal shape peaking at $\rho_{\rm gas} \sim 10^{-26}$ g cm^{-3}. However, in the RTCRiMHD model, the escaping gas features higher densities that reach the intermediate range ($\rho_{\rm gas} \sim 10^{-26} - 10^{-24}$ g cm^{-3}), with comparable fall-offs towards both higher and lower densities. This is due to the denser and smoother outflows produced by CRs (P. Girichidis et al. 2018; see also the projection in Fig. 1). The RTCRiMHD simulations has gas densities $\rho_{\rm gas} < 10^{-28}$ g cm^{-3} only at very specific times, such as shortly after its SF burst at $z \sim 5$. Additionally, our 'full-physics' simulation is the only model that features escaping gas at $\rho_{\rm gas} > 10^{-24}$ g cm^{-3}. At even higher densities, gas with positive radial velocities becomes only outflowing (rather than escaping; orange histograms).

The right column in Fig. 5 shows the distribution of gas mass fraction as a function of temperature, where most of the mass sits between 10^2 K $\lesssim T \lesssim 10^7$ K. The PDFs indicate a significant fraction of cold, dense gas in star forming regions ($T \sim 10^2$ K; e.g. HD, RTCRiMHD), a concentration of gas around the thermally stable $T \sim 10^4$ K, and a long tail towards high temperatures above $T \gtrsim 10^5$ K. Including stellar radiation leads to a smoother distribution between ($T \sim 10^4 - 3 \times 10^4$ K), accentuated by hydrogen photoionization and photoheating. Stellar radiation also reduces the proportion of gas at $T < 100$ K which is present at almost all times with non-zero SFR, due to rapid evaporation of giant gas clouds from early stellar feedback. Including CRs increases the proportion of gas at $T \lesssim 500$ K, with a much lower fraction of low temperature gas being inflowing at $T \lesssim 10^4$ K.

Across all our models, we find most gas at temperatures above 10^6 K to be escaping (i.e. $v_{\rm r} > v_{\rm esc}$) as this gas is heated by SN explosions. Including radiation reduces the proportion of escaping gas, and entrains a higher relative proportion of gas at lower temperatures ($T \sim 10^5$ K). Combining stellar radiation with CRs yields a large proportion of outflowing and escaping gas. Notably, the escaping gas also has significantly lower temperatures, with some of the gas heated by stellar radiation now entrained in escaping outflows ($T \sim 3 \times 10^4$ K), leading to a more multiphase nature of the outflows. We find for the RTCRiMHD model an average ~ 15 per cent (and a median of ~ 5 per cent) of the outflow mass to be neutral gas, although there are large variation across cosmic time (with some snapshots having neutral-mass dominated outflows). This is in better agreement with multiphase and neutral gas observations (e.g. Y. M. Chen et al. 2010; A. Fluetsch et al. 2019; I. Schroetter et al. 2019; S. Veilleux et al. 2020; F. D'Eugenio et al. 2023; M. Romano et al. 2023, albeit mostly of more massive galaxies). This result is particularly notable when comparing with the HD + Boost case, for which the outflows feature exceptionally high temperatures, and are virtually dominated by the hot and ionized gas phase. The mass-loading in different phases is further discussed and compared with observations in the next section.

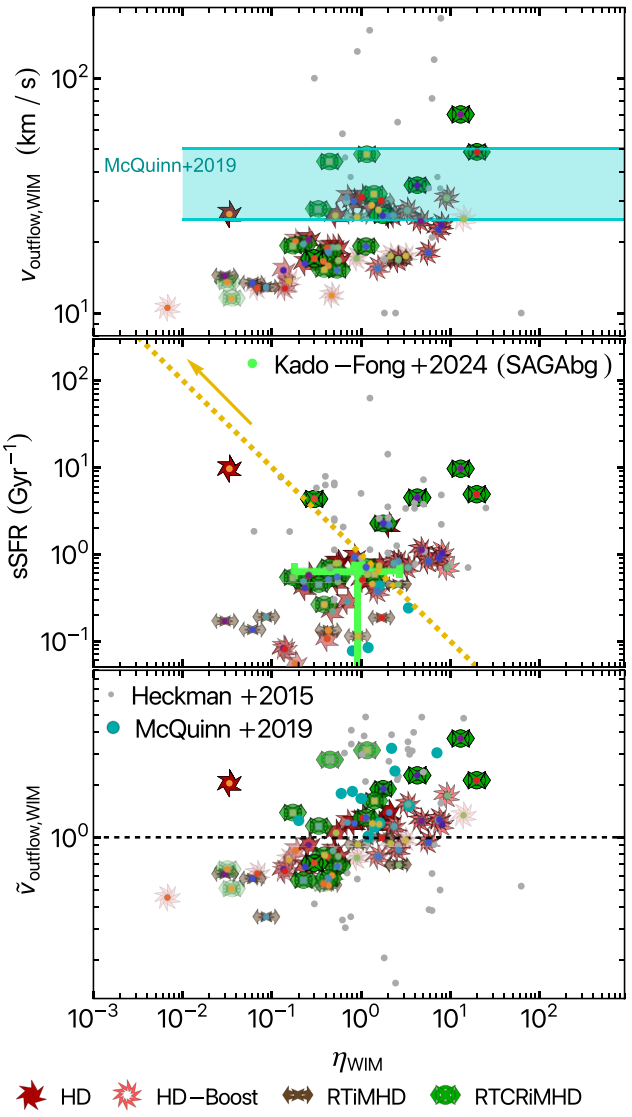

Figure 6. Intrinsic (simulated) properties of the warm ionized outflows for the Pandora dwarf galaxy. From top to bottom, panels display the following quantities as a function of the WIM mass-loading factor: the mass-weighted WIM gas outflow velocity, $v_{\rm outflow,\,WIM}$, the sSFR over the last 100 Myr; and a dimensionless velocity ratio $\tilde{v}_{\rm outflow,\,WIM} = v_{\rm outflow,\,WIM}/v_{\rm circ}$. Different datapoints from our simulations correspond to different snapshots in the interval of $3.5 < z < 5$. Snapshots featuring considerably lower star formation rates are displayed with lower opacity symbols. The gold coloured line in the central panel indicates increasing SFR for a fixed outflow and stellar mass. We overlay as coloured circles the redshift of the models, ranging from high redshift (blue) to low redshift (red). We find no clear systematic trends across the studied period. The inclusion of radiation which acts as an early stellar feedback process results in slower and weaker outflows. However, when CR feedback is incorporated as well, WIM has much larger outflow velocities and mass-loading factors. Fig. 7 shows comparable quantities, measured instead following an observation-like procedure for H α emission.

3.4 Comparing the properties of the Pandora suite with observations

3.4.1 Warm and ionized outflow mass-loadings and velocities

We now turn to investigate how the different outflow properties we measure in the simulations compare with the observed properties of ionized gas. The separation into ionized and neutral gas is computed through a simple separation according to the hydrogen ionization fraction $x_{\rm HII}$: neutral gas density, $\rho_{\rm HI} = \rho_{\rm gas}(1 - x_{\rm HII})$, and ionized gas density, $\rho_{\rm HII} = \rho_{\rm gas} x_{\rm HII}$. In Fig. 6, where we focus on intrinsic quantities as directly calculated from the simulations, we show how the mass-loading factor of warm ionized medium (WIM) varies

across our models during the $z \in [5, 3.5]$ interval.[5] We classify cells to be within the WIM and WNM temperature range when they fulfill 200 K $< T \leq 10^6$ K, with their gas mass contributing proportionally to their ionization fraction. From top to bottom, panels show the mass-weighted WIM gas outflow velocity $v_{\rm outflow,\,WIM}$, the specific SFR (sSFR) measured in a time window of 100 Myr, and a dimensionless velocity ratio $\tilde{v}_{\rm outflow,\,WIM}$. This quantity measures the relevance of outflow velocities versus the characteristic circular velocity, $v_{\rm circ}$, of the system as $\tilde{v}_{\rm outflow,\,WIM} = v_{\rm outflow,\,WIM}/v_{\rm circ}$. We measure $v_{\rm outflow,\,WIM}$ and the $\eta_{\rm WIM}$ factor at $0.2\,r_{\rm halo}$. Each data point corresponds to a different snapshot, displayed with higher opacities when the SFR is higher. We also indicate the redshift evolution by including coloured circles in each of our data points, ranging from high redshift (blue; $z \sim 5$) to low redshift (red; $z \sim 3.5$). These provide some guidance on whether any systematic trends emerge across the studied period. We find that there are no apparent trends beyond those driven by the temporal variations of the SFR.

The panels show outflows to have the highest mass-loading factors in the HD + Boost and RTCRiMHD models, typically with $\eta_{\rm WIM} \sim$ 1–10 for moderate star formation events. The RTiMHD model has the lowest mass-loading factors overall, with $\eta_{\rm WIM} \sim 0.1$–1. These mass-loading factors reflect our previous results, where radiation dampens the mass-loading of the outflows while CRs increase it. The mass-weighted warm ionized gas outflow velocities, $v_{\rm outflow,\,WIM}$, shown in the first panel, vary significantly across our different models. The HD and HD + Boost simulations have outflows with relatively narrow velocity ranges, $v_{\rm outflow,\,WIM} \sim 15$–$30$ km s^{-1}. The velocities in the RTiMHD model with radiation are reduced to $\sim$15 km s^{-1}. The RTCRiMHD model has the highest mass-weighted outflow velocities, at times reaching ~ 70 km s^{-1}. Perhaps with the exception of the RTiMHD model, all the models show reasonable agreement with the outflow velocities inferred by the local observations by T. M. Heckman et al. (2015) and those assumed by K. B. McQuinn et al. (2019), included in the figure for reference.[6]

The second panel of Fig. 6 shows the relation between $\eta_{\rm WIM}$ and the sSFR, where all our models feature some degree of the expected positive correlation between increasing sSFR and $\eta_{\rm WIM}$ – a larger fraction of mass is ejected as the relative importance of the ongoing SFR with respect to the galaxy mass increases. To aid interpretation we include a dashed golden line of constant stellar and outflow mass, with the arrow indicating increasing SFR. Overall, all our models display this positive correlation of higher outflow rates for higher sSFR. The HD and HD + Boost models have comparable sSFR values, typically of the order of 1 Gyr^{-1} whenever WIM outflows are present, and lower otherwise. The RTiMHD has somewhat lower sSFR values $\lesssim 0.5$ Gyr^{-1} and outflow rates. RTCRiMHD displays higher WIM outflow mass-loading factors, as well as higher sSFR, spanning a larger dynamical range, attributed to its higher star formation burstiness. This supports the connection between high star formation burstiness, feedback, and galactic outflows (S. Carniani et al. 2024), and poses non-thermal physics as an important regulator of their interplay. Notably, the bulk of our galaxy measurements is in very good agreement with the inferred mass-loading factors by T. M. Heckman et al. (2015) as well as E. Kado-Fong et al. (2024) which employ background galaxies (SAGAbg) observed by the SAGA Survey (M. Geha et al. 2017).

As shown in S. Martin-Alvarez et al. (2023), our different galaxy formation models lead to distinct predictions for the dynamical masses and sizes of the resulting galaxy. Mass and size of the galaxy are thereby related to the circular velocity as $v_{\rm circ} = \sqrt{GM/r}$. To estimate the relevance of outflow velocity per system, we propose the following diagnostic: a dimensionless $\tilde{v}_{\rm outflow,\,WIM}(r = 0.2\,r_{\rm halo}) = v_{\rm outflow,\,WIM}/v_{\rm circ}(r)$ against the dimensionless mass-loading factor, shown in the bottom panel of Fig. 6. We include a dashed horizontal black line at $\tilde{v}_{\rm outflow,\,WIM} = 1$ to separate the low and high $\tilde{v}_{\rm outflow,\,WIM}$ regimes. This plot highlights how the models studied here separate in the $\tilde{v}_{\rm outflow,\,WIM} - \eta_{\rm WIM}$ parameter space: at low mass-loading factors ($\eta_{\rm WIM} < 1$), all models are comparable, with outflowing gas moving at relatively low characteristic speeds ($\tilde{v}_{\rm outflow,\,WIM} \sim 0.8$). However, as $\eta_{\rm WIM}$ increases, we find outflows with comparatively different characteristic velocity ratio $\tilde{v}_{\rm outflow,\,WIM}$. The RTiMHD simulation not only typically has the lowest mass-loading, but also the slowest $\tilde{v}_{\rm outflow,\,WIM}$. In agreement with our previous findings, HD reaches intermediate values for both the high end of $\tilde{v}_{\rm outflow,\,WIM}$ and $\eta_{\rm WIM}$. Notably, while both HD + Boost and RTCRiMHD reach the highest $\eta_{\rm WIM}$ values, RTCRiMHD has the highest $\tilde{v}_{\rm outflow,\,WIM}$ overall. Hence, the $\tilde{v}_{\rm outflow,\,WIM}(\eta_{\rm WIM})$ parameter space predicts different outflow properties for thermal versus non-thermal galaxy formation models allowing to observationally differentiate models.

3.4.2 Observation-like measurement of ionized outflows

Various observational studies extract the properties of galaxy outflows from the analysis of emission line profiles (e.g. A. Fluetsch et al. 2021; A. Marasco et al. 2023; S. Carniani et al. 2024). By modelling these as a combination of Gaussian components, the broad component can be identified as associated with the gas outflowing from galaxies. The integral of its emission (or in some models, only a fraction of its phase space, e.g. A. Marasco et al. 2023) is then related to the outflowing mass $M_{\rm outflow}$, and its full-width-at-half-maximum (FWHM) to the outflow velocity, which we label $v_{\rm broad}$. These two quantities and the estimate for the size of the galaxy $r_{\rm galaxy}$, allow measuring the outflow rate as

$$\dot{M}_{\rm outflow} = \frac{M_{\rm outflow}\, v_{\rm broad}}{r_{\rm galaxy}}. \tag{1}$$

In this section, we follow a simple procedure aimed to follow such studies to estimate observation-like outflow properties. We outline the key steps, and highlight the most important caveats. A more detailed discussion about these is provided in Appendix C.

For each galaxy, we compute the H α emission (estimated following H. Katz et al. 2022) line profile accordingly to the line-of-sight velocity for 12 uniformly distributed directions. We fit a double Gaussian to the line profiles, and associate the broad component with the outflowing gas. Following D. S. Rupke, S. Veilleux & D. B. Sanders (2005), the outflow velocity $v_{\rm broad}$ is frequently defined as

$$v_{\rm broad} = \frac{\rm FWHM_{broad}}{2} + \Delta v, \tag{2}$$

where $\rm FWHM_{broad}$ is the FWHM of the broad component, and Δv is the difference between the two components mean velocity. This velocity is often associated to the 95$^{\rm th}$ percentile of the velocity distribution (which we confirm in Fig. C2), but does not necessarily correspond to the outflowing gas mass-weighted velocity (see Appendix C). The outflow mass is extracted from the total luminosity of the broad component, $L_{\rm H\,\alpha,\,broad}$, following the relation employed

[5] For observation-like analysis of the WIM and WNM outflows see Sections 3.4.2 and 3.4.3.

[6] We note here that our simulations are of a dwarf galaxy at high redshift, while these observations are of local dwarfs. This qualitative comparison is intended for systems of similar mass and SFR, and does not inform us about the cosmological evolution of dwarf galaxies.

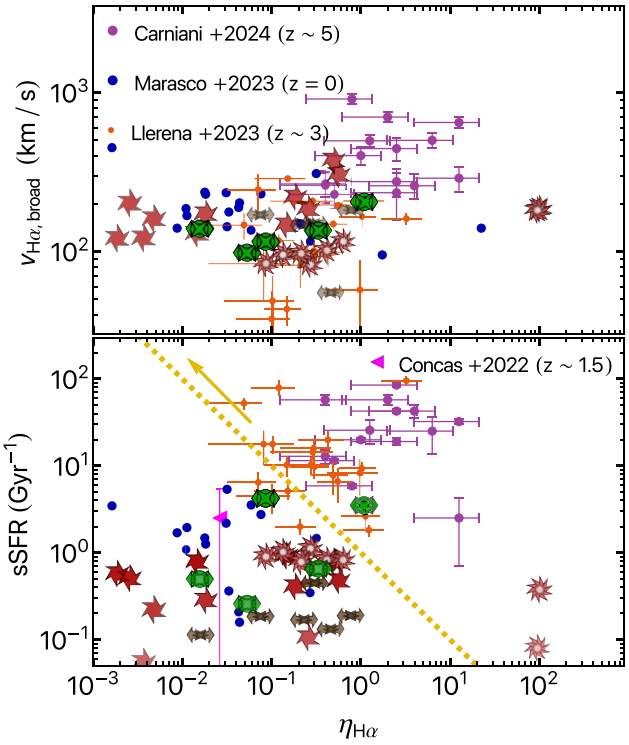

Figure 7. Observation-like properties of the ionized outflows for our simulated galaxy, as measured from synthetic H α line profiles. The top panel displays the outflow velocity $v_{H\alpha,\,broad}$ measured from the broad component of the line, a proxy for the 95th percentile of the WIM velocity; whereas the bottom panel shows the sSFR over the last 100 Myr. Both are shown as a function of the observationally inferred mass-loading factor, $\eta_{H\alpha}$ (see Appendix C for estimation of $v_{H\alpha,\,broad}$ and $\eta_{H\alpha}$). Our measurements are compared with observational results inferring outflow properties through the methodology we emulate, spanning from low ($z = 0$, A. Marasco et al. 2023; $z \sim 1.5$, upper limit/non-detection for the low-stellar mass bin by A. Concas et al. 2022), to high ($z \sim 3$, M. Llerena et al. 2023; $z \sim 5$, S. Carniani et al. 2024) redshift. Overall, we find most of our simulated models to be in broad agreement with observations for the overlapping range of stellar masses.

by A. Concas et al. (2022) and A. Marasco et al. (2023)

$$M_{outflow} = 3.2 \times 10^5 \frac{L_{H\alpha,\,broad}}{10^{40}\,erg\,s^{-1}} \left(\frac{100\,cm^{-3}}{n_e}\right) M_\odot, \quad (3)$$

where n_e is the electron number density. Here, we follow observations and assume $n_e \sim 300\,cm^{-3}$, although we note that the typical outflow densities in our simulations are lower and that n_e has a clear radial gradient.[7] Finally, we set r_{galaxy} as twice the half-mass radius r_*.

Following this procedure, we obtain the mass-loading factors, $\eta_{H\alpha}$, and compare this with the observation-like outflow velocity, $v_{H\alpha,\,broad}$, and the sSFR[8] in Fig. 7. Overall, we find $v_{H\alpha,\,broad}$ to be similar across our models, with values in reasonable agreement with both the observations at low-redshift by A. Marasco et al. (2023) and at high-redshift ($z \sim 3$) by M. Llerena et al. (2023). The velocities inferred by S. Carniani et al. (2024) at $z \sim 5$ are somewhat higher ($\gtrsim 200$ km s^{-1}), although their stellar masses and sSFR are also higher ($M_* \gtrsim 5 \times 10^7\,M_\odot$ compared with our $M_* \lesssim 10^7\,M_\odot$). We, however, stress that our mock outflow velocities $v_{H\alpha,\,broad}$ and their trend with the mass-loading factor are not an accurate reflection of mass-weighted WIM outflows as directly calculated from our simulations.[9] All of our models compare reasonably well with observations in the sSFR–$\eta_{H\alpha}$ relation. By reaching higher sSFR values in some snapshots, the RTCRiMHD model is also comparable with some higher redshift observations, although further sampling than provided by our simulations will be required. Building up on this apparent agreement for most of our models with observations of ionized outflows, we highlight the importance of forward-modelling the simulation results to bridge the gap when comparing with observations. This enables to better constrain the models as well as to infer the 'true' outflow properties from observations. Doing this causes non-negligible variations that reduce our mass-loading factors and increase the outflow velocities with respect to our results in Fig. 6. In future work we plan to employ more sophisticated forward-modelling techniques, and expand on this analysis with the larger sample of galaxies from the Azahar simulations (S. Martin-Alvarez et al. 2025).

3.4.3 *Neutral outflow mass-loadings and velocities*

As shown above, galaxy winds in the presence of CRs entrain a larger proportion of denser and more temperate gas (see also e.g. P. Girichidis et al. 2018; G. Dashyan & Y. Dubois 2020; P. F. Hopkins et al. 2021; M. Farcy et al. 2022; F. Rodríguez Montero et al. 2024). We analyse the capability of ejecting warm neutral medium (WNM) outflows from the simulated dwarf galaxy in Fig. 8, which shows from top to bottom, the $v_{WNM,\,broad}$, the mass-weighted WNM outflow velocity, and the sSFR as a function of the WNM mass-loading factor. The RTCRiMHD model is particularly effective at driving WNM outflows, with $\eta_{WNM} \sim 10^0 - 10^1$, significantly higher than for our purely hydrodynamical simulations (HD and HD + Boost). Beyond the pressure gradients associated with non-thermal processes – which provide a mechanism to drive denser gas outflows without heating them to higher temperatures – the RT-driven local photoheating of gas (bottom panel of Fig. 3) also increases the fraction of partially ionized gas at $T \lesssim 3 \times 10^4$ K which is entrained in outflows. In the RTCRiMHD model our dwarf galaxy exhibits a higher fraction of events with larger $v_{WNM,\,broad}$ values, which are in reasonable agreement with the observations by M. Romano et al. (2023). While $v_{WNM,\,broad}$ is comparable or somewhat higher for the RTCRiMHD model, the mass-weighted outflow velocity in this model is lower than in the thermally-dominated feedback models, reflecting a higher proportion of the ejected mass that is moving at lower velocities. Finally, by examining the sSFR–η_{WNM} relation, we find that the combination of burstiness in the RTCRiMHD model with its higher η_{WNM} leads to a good agreement with the observations by M. Romano et al. (2023), highlighting how observations of neutral outflows can help discriminate between models featuring different non-thermal physical processes.

[7] These assumptions about n_e may bias our $M_{outflow}$ measurements low, and is further discussed in Appendix C.

[8] For consistency we maintain the sSFR measured in the same time window of 100 Myr, but note that measuring the SFR over shorter time periods may reveal higher peaks of SFR, particularly for higher burstiness models. This would shift the simulated data points along the golden dashed line in the sSFR – η panels as indicated by the arrow. Detailed comparisons with different observations may require adjusting the timescale accordingly to the specific observational SFR tracer.

[9] The HD model appears to have somewhat higher $v_{H\alpha,\,broad}$ than the other models. We also note that HD also has a higher amount of valid double Gaussian fits.

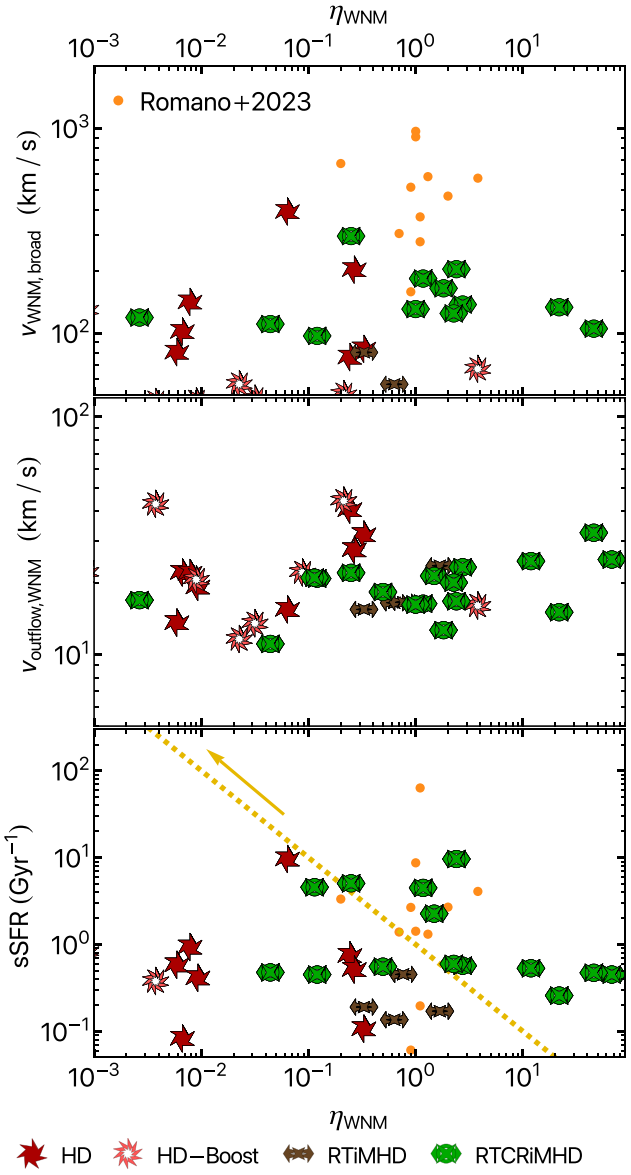

Figure 8. From top to bottom, panels display $v_{WNM,\,broad}$ (a proxy for the 95th percentile of the WNM velocity distribution), the mass-weighted WNM outflow velocity $v_{outflow,\,WNM}$, and the sSFR. All quantities are shown as a function of the WNM mass-loading factor η_{WNM}, directly measured from the simulations. The RTCRiMHD model is capable of driving temperate outflows with considerably higher neutral gas mass-loading factors than its purely hydrodynamical counterparts, and is in good agreement with the observations by M. Romano et al. (2023).

Finally, we note that we measure only a very small proportion of cold neutral outflows (used as a proxy for molecular outflows; $T \leq 200$ K), and mostly only present in the RTCRiMHD model. Whether such outflows in dwarf galaxies, which already feature low CO detections (A. Schruba et al. 2012), may only be driven by AGN (M. Mezcua et al. 2016), or are even not expected (C. Barfety et al. 2025) remains to be understood.

3.4.4 *Galaxy stellar metal enrichment and gas outflow metallicities*

Another important galactic property that is notably affected by galactic outflows is metal enrichment, as the primary source of enrichment is the SN feedback that is also responsible for accelerating such outflows. The left panel of Fig. 9 shows how the stellar metal enrichment of the simulated galaxies vary across our models, whereas the right column of panels provides further detail on the outflowing gas metallicity. Focusing first on the left panel, we show the average stellar metallicity for the Pandora suite compared with Local Group observations (E. N. Kirby et al. 2013), higher redshift *JWST* observations of gas metallicities in large dwarf galaxies by M. Curti et al. (2024; we restrict the comparison to their data at $3 < z < 4$) and smaller dwarfs (at $6 < z < 8$) by I. Chemerynska et al. (2024). We show extrapolated metallicities for low-redshift (C. A. Tremonti et al. 2004) and high-redshift (D. K. Erb et al. 2006) *SDSS* observations. See also e.g. H. J. Zahid et al. (2013) and M. Curti et al. (2020) for additional mass–metallicity relations across redshifts. We also include predictions at $z \sim 3.5$ from the high-resolution cosmological simulation New Horizon (Y. Dubois et al. 2021), and from IllustrisTNG (P. Torrey et al. 2019) to contextualize our simulations. Due to the expected lack of growth and enrichment evolution of the galaxy down to $z \sim 0$ (S. Martin-Alvarez et al. 2023; see also low-z measurements in Appendix D), comparisons to low redshift data are insightful. Such comparison is particularly relevant when considering recent findings by M. Curti et al. (2024), indicating low-mass galaxies exhibit metallicities comparable to local analogues such as 'Blueberry' and 'Green Pea' galaxies (H. Yang et al. 2017a, b).

All of our models have stellar metallicities that match observational data, with the exception of the model with enhanced feedback, HD + Boost, which leads to metallicities significantly lower than observed, as most of its metals are ejected from the galaxy. This emphasizes that stellar metallicity is a powerful diagnostic tool for distinguishing between different galaxy formation models. We briefly describe how the larger sample of Pandora models occupies this enrichment space in Appendix D. The right-hand panels of Fig. 9 showcase the metallicity distribution of the gas in the galaxy (black), separated into outflowing (orange) and escaping (red) gas following the same approach as for Fig. 5. We include vertical dashed lines corresponding to the average metallicities of the stellar component (green line), total gas component (black line), the outflowing gas (golden line), and the escaping gas (pink line). Across most models, the average stellar metallicity is comparable to that of the outflowing gas, with the notable exception of the HD + Boost simulation. This disparity emerges from the too efficient ejection of metals from the galaxy after 'boosted' SN feedback events, which in turn restricts the increase of the stellar metallicity, leading to the disagreement with observations. This overefficient ejection of metals is showcased by the PDF of escaping gas, which contains virtually all gas with $Z > \langle Z_* \rangle$ in HD + Boost. Instead, the models featuring Z_* comparable to observations are capable of retaining some of their enriched gas with $Z \sim \langle Z_* \rangle$. The HD and HD + Boost models have comparable metallicity distributions shapes for outflowing and escaping gas at $Z > \langle Z_* \rangle$. This is due to their explosive, single acceleration mechanism through SNe. In contrast, the non-thermal physics models have more differentiated outflowing and escaping gas PDFs at $Z \gtrsim \langle Z_* \rangle$. This is not only due to non-thermal pressures contributing to gas acceleration, but also to different local small-scale environmental properties around SN events (Fig. 3). In addition to having denser and more temperate escaping outflows, RTCRiMHD escaping outflows also have a heterogeneous mixture of different metallicities, interestingly also containing a non-negligible fraction of low-metallicity material. Our findings confirm metal enrichment observations of dwarf galaxies as valuable diagnostics to distinguish not only outflow driving mechanisms, but also the physics of

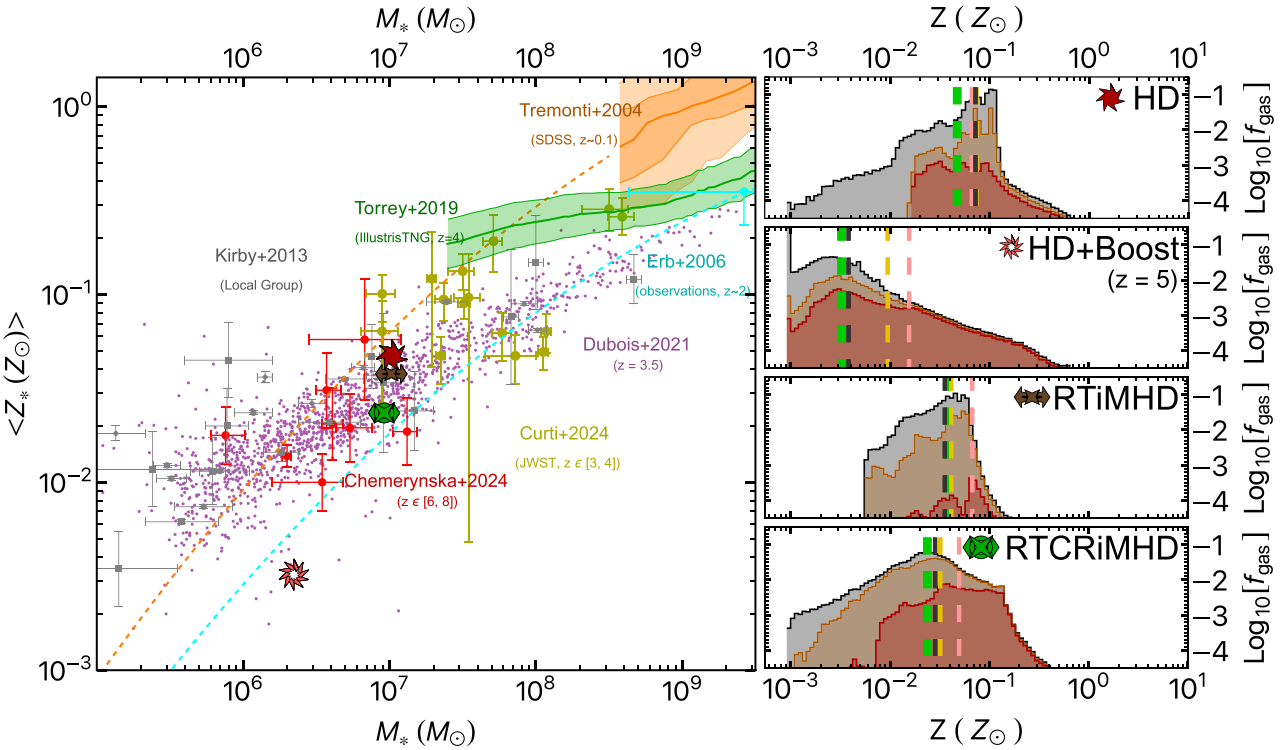

Figure 9. Left panel: Stellar mass–stellar metallicity relation of the Pandora dwarf galaxy at $z = 3.5$ for our different models. We show for comparison local dwarf galaxies observations (grey points) by E. N. Kirby et al. (2013) as well as higher redshift observations employing *JWST* by M. Curti et al. (2024) at $3 < z < 4$ (yellow points) and I. Chemerynska et al. (2024) at $6 < z < 8$ (red points). We include *SDSS* data of galaxies with larger stellar masses at low (C. A. Tremonti et al. 2004; orange bands) and high ($z \sim 2$, D. K. Erb et al. 2006) redshift (cyan points and cyan dashed line). We also show data for the New Horizon ($z = 3.5$, violet data points; Y. Dubois et al. 2021) and IllustrisTNG ($z = 4$, green band; P. Torrey et al. 2019) simulations for comparison. Most of our models provide a reasonable match to observations, except the 'boosted' feedback model HD + Boost. Right column panels: Gas mass metallicity PDFs, with gas (black distribution) separated into outflowing (orange) and escaping (red) as done in Fig. 5. Vertical dashed lines correspond to the average stellar (green), gas (black), outflowing (gold) and escaping (pink) metallicities. The RTCRiMHD simulation has a large fraction of escaping gas which is highly metal enriched, as well as a significant outflowing component that has a broad range of metallicities.

galaxy formation models more generally. In upcoming work (Martin-Alvarez et al. in preparation) we will address how different galaxy formation models affect the spatial distribution of such metallicities (Fig. 1, where observables such as metallicity gradients having the potential to further constrain dwarf galaxy formation models (e.g. S. W. Fu et al. 2024a, b). Complementarily, galaxy outflows from dwarf galaxies drive the observational signatures of their CGM enrichment (J. K. Werk et al. 2014; J. X. Prochaska et al. 2017; F. Li et al. 2020; Y. Zheng et al. 2024), serving as a further constraint on galaxy formation models with different outflow characteristics.

4 CONCLUSIONS

In this work, we investigate the interplay between star formation, stellar feedback, galaxy outflows, and metal enrichment in dwarf galaxies. We analyse a representative subset of the Pandora galaxy formation models (S. Martin-Alvarez et al. 2023), focusing on a high-resolution ($\Delta x \sim 7$, pc) cosmological zoom-in simulation of a dwarf galaxy with halo mass $M_{\rm vir}(z = 0) \approx 10^{10}$ M$_\odot$. The models studied include: a standard hydrodynamic simulation (HD), a 'boosted' SN feedback model (HD + Boost), a model with magnetohydrodynamics and stellar radiation via radiative transfer (RTiMHD), and a 'full-physics' simulation incorporating stellar radiation, magnetic fields, and cosmic rays (RTCRiMHD).

We examine how the star formation history – and in particular, its burstiness – influences the galaxy's ability to launch outflows, and how this is modulated by the local environments of SN explosions. We further study how different forms of non-thermal pressure shape the properties of outflowing and escaping gas. Finally, we compare our simulation results to observations of galaxy-scale outflows and metal enrichment. Our main findings can be summarized as follows:

(i) The star formation history of the dwarf galaxy is highly sensitive to the included physics. In the standard hydrodynamic model (HD), star formation proceeds continuously with mild SN-driven variability. Adding radiation smooths these short-time-scale fluctuations by suppressing small-scale clustering. When cosmic rays are included, star formation becomes episodic and strongly bursty – more so even than in the 'boosted' SN feedback model. These results align with recent *JWST* observations that reveal bursty, mini-quenched, and rejuvenated star formation in low-mass galaxies (e.g. R. Endsley et al. 2024; T. J. Looser et al. 2024; W. M. Baker et al. 2025; T. Dome et al. 2025; C. Witten et al. 2025).

(ii) The distribution of SN explosion environments reveals a density and temperature bimodality across models, reflecting explosions in both dense star-forming clouds and low-density, pre-processed gas. In the 'boosted' SN model, even a few clustered explosions efficiently disperse dense gas, reducing the number of SNe in high-density regions. In contrast, the inclusion of radiative transfer reduces SN clustering, leading to more explosions in dense and photoheated environments. The 'full-physics' model shows a similar distribution to the standard case (HD), but with SNe occurring at slightly

higher densities in the diffuse ISM while retaining the characteristic photoheating temperature peak.

(iii) Thermal pressure dominates the overall gas support across the halo, but cosmic rays provide significant additional pressure within the central region ($r < 0.2, r_{\rm halo}$), especially during strong outflow events. Beyond this radius, radiation pressure becomes increasingly important and contributes to thermal heating in the circumgalactic medium. Magnetic pressure is generally subdominant but can locally dominate in dense star-forming clouds within the galaxy's innermost regions.

(iv) Cosmic ray feedback drives dense, fast, and mass-loaded outflows that include a significant neutral gas component and span a broader range of temperatures and metallicities. Despite injecting less total energy than the 'boosted' SN model, this 'full-physics' run produces more efficient outflows – highlighting the critical role of cosmic rays in shaping multiphase winds. Future observations that can constrain the multiphase nature of outflows both from local and high redshift dwarfs will be instrumental in validating our predictions.

(v) Observable properties of ionized gas outflows – particularly the relation between mass-loading factor and normalized mass-weighted outflow velocity (e.g. $v_{\rm out}/v_{\rm circ}$) – provide a powerful diagnostic for distinguishing between feedback models. Under our simple observation-like analysis – employing H α line profiles – all our models are in reasonable agreement with observations (A. Concas et al. 2022; M. Llerena et al. 2023; A. Marasco et al. 2023; S. Carniani et al. 2024). Among our simulations, the 'full-physics' model best matches observed trends in both local and high-redshift galaxies, and especially for observations of neutral outflows. This suggests that cosmic ray feedback plays a key role in shaping realistic outflows.

(vi) Except for the 'boosted' SN model, all Pandora simulations yield stellar metallicities consistent with observations of both local and high-redshift dwarf galaxies (E. N. Kirby et al. 2013; I. Chemerynska et al. 2024; M. Curti et al. 2024). The 'full-physics' model produces denser, more temperate outflows with a wide range of metallicities – from $\sim 10^{-3} Z_{\odot}$ to $\sim 0.4 Z_{\odot}$ – revealing the chemically complex nature of dwarf galaxy outflows and their significant contribution to CGM enrichment.

Our findings underscore the fundamental importance of incorporating non-thermal physics – stellar radiation, magnetic fields, and cosmic rays – into models of galaxy formation. These processes are essential for regulating star formation, driving multiphase outflows, and shaping the chemical enrichment of galaxies.

The emerging picture from our simulations is one in which non-thermal pressures and early stellar feedback critically shape the smallest galactic systems. This has exciting implications for upcoming multiwavelength observatories such as *JWST*, the upcoming extremely large telescopes (ELT, GMT, TMT), SKAO, ngVLA, and Roman, which will enable more detailed studies of the kinematics, thermodynamics, and metal content of galaxy outflows. In particular, measurements of outflow velocities and metallicities across gas phases offer a sensitive means to distinguish between competing models of galaxy formation and feedback. Our results show that forward-modelling the observational process leads to better agreement on a face-value comparison with observed trends than using intrinsic simulation quantities. This highlights how sophisticated synthetic observation analysis will be fundamental to understand these upcoming panchromatic observations. To extend this work, our upcoming high-resolution Azahar cosmological simulation suite (S. Martin-Alvarez et al. 2025; Martin-Alvarez et al., in preparation) will systematically explore a broad range of galaxy masses, incorporating these new physical prescriptions. These simulations will provide new insight into how radiative transfer, cosmic rays, and magnetic fields shape galaxy evolution across cosmic time.

ACKNOWLEDGEMENTS

The authors kindly thank the referee for their careful consideration of this manuscript, and their insightful comments and suggestions, which have highly improved the quality of this manuscript. This research was supported by the Kavli Institute for Particle Astrophysics and Cosmology. We would like to thank Dalya Baron, Jaeyeon Kim, and Sal Fu for useful comments and discussions. SMA is supported by a Kavli Institute for Particle Astrophysics and Cosmology (KIPAC) Fellowship, and by the NASA/DLR Stratospheric Observatory for Infrared Astronomy (SOFIA) under the 08_0012 Program. SOFIA is jointly operated by the Universities Space Research Association, Inc. (USRA), under NASA contract NNA17BF53C, and the Deutsches SOFIA Institut (DSI) under DLR contract 50OK0901 to the University of Stuttgart. SMA also acknowledges visitor support from the Kavli Institute for Cosmology, Cambridge, where part of this work was completed. DS acknowledges support by European Research Council Starting Grant 638707 'Black holes and their host galaxies: coevolution across cosmic time'. DS and MH additionally acknowledge support from the Science and Technology Facilities Council (STFC; grant number ST/W000997/1). MF acknowledges funding from the Swiss National Science Foundation (SNF) via a PRIMA Grant PR00P2 193577 'From cosmic dawn to high noon: the role of black holes for young galaxies'. MS acknowledges the support from the Swiss National Science Foundation under Grant No. P500PT_214488. FRM was supported by funds provided by the Kavli Institute for Cosmological Physics at the University of Chicago through an endowment from the Kavli Foundation.

This work used the DiRAC@Durham facility managed by the Institute for Computational Cosmology on behalf of the STFC DiRAC HPC Facility (www.dirac.ac.uk). The equipment was funded by BEIS capital funding via STFC capital grants ST/P002293/1, ST/R002371/1, and ST/S002502/1, Durham University and STFC operations grant ST/R000832/1. DiRAC is part of the National e-Infrastructure. Some of the computing for this project was performed on the Sherlock cluster. We would like to thank Stanford University and the Stanford Research Computing Center for providing computational resources and support that contributed to these research results. This work was performed using resources provided by the Cambridge Service for Data Driven Discovery (CSD3) operated by the University of Cambridge Research Computing Service (www.csd3.cam.ac.uk), provided by Dell EMC and Intel using Tier-2 funding from the Engineering and Physical Sciences Research Council (capital grant EP/P020259/1), and DiRAC funding from the Science and Technology Facilities Council (www.dirac.ac.uk).

DATA AVAILABILITY

The data employed in this manuscript is to be shared upon reasonable request contacting the corresponding author.

REFERENCES

Ackermann M. et al., 2012, ApJ, 755, 164
Agertz O., Teyssier R., Moore B., 2009, MNRAS, 397, L64
Agertz O., Kravtsov A. V., Leitner S. N., Gnedin N. Y., 2013, ApJ, 770, 25
Agertz O. et al., 2020, MNRAS, 491, 1656
Armillotta L., Ostriker E. C., Jiang Y.-F., 2021, ApJ, 922, 11

Armillotta L., Ostriker E. C., Kim C.-G., Jiang Y.-F., 2024, ApJ, 964, 99
Bahé Y. M. et al., 2017, MNRAS, 470, 4186
Baker W. M. et al., 2025, A&A, 814, 803
Barfety C. et al., 2025, ApJ, 988, 55
Baron D., Netzer H., Lutz D., Davies R. I., Prochaska J. X., 2024, ApJ, 968, 23
Bennett J. S. et al., 2025, MNRAS, 543, 1456
Bogdan A. et al., 2013, ApJ, 772, 97
Booth C. M., Agertz O., Kravtsov A. V., Gnedin N. Y., 2013, ApJ, 777, L16
Borlaff A. S. et al., 2023, ApJ, 952, 4
Broderick A. E., Tiede P., Chang P., Lamberts A., Pfrommer C., Puchwein E., Shalaby M., Werhahn M., 2018, ApJ, 868, 87
Brooks A. M., Governato F., Booth C. M., Willman B., Gardner J. P., Wadsley J., Stinson G., Quinn T., 2007, ApJ, 655, L17
Buck T., Pfrommer C., Pakmor R., Grand R. J., Springel V., 2020, MNRAS, 497, 1712
Bullock J. S., Boylan-Kolchin M., 2017, ARA&A, 55, 343
Butsky I. S., Quinn T. R., 2018, ApJ, 868, 108
Butsky I. S., Nakum S., Ponnada S. B., Hummels C. B., Ji S., Hopkins P. F., 2023, MNRAS, 521, 2477
Carniani S. et al., 2024, A&A, 685, A99
Chemerynska I. et al., 2024, ApJ, 976, L15
Chen Y. M., Tremonti C. A., Heckman T. M., Guinevere K., Weiner B. J., Jarle B., Jing W., 2010, AJ, 140, 445
Cherrey M. et al., 2025, A&A, 694, A117
Chisholm J., Matsushita S., 2016, ApJ, 830, 72
Chisholm J., Tremonti C. A., Leitherer C., Chen Y., Wofford A., Lundgren B., 2015, ApJ, 811, 149
Chisholm J., Tremonti C. A., Leitherer C., Chen Y., 2017, MNRAS, 469, 4831
Choi B.-E., Werk J. K., Tchernyshyov K., Prochaska J. X., Zheng Y., Putman M. E., Fielding D. B., Strader J., 2024, ApJ, 976, 222
Commerçon B., Marcowith A., Dubois Y., 2019, A&A, 622, A143
Concas A., Popesso P., Brusa M., Mainieri V., Thomas D., 2019, A&A, 622, A188
Concas A. et al., 2022, MNRAS, 513, 2535
Cummings A. C. et al., 2016, ApJ, 831, 18
Curti M. et al., 2020, MNRAS, 492, 821
Curti M. et al., 2024, A&A, 684, A75
D'Eugenio F. et al., 2023, Nat. Astron., 8, 1443
Dacunha T., Martin-Alvarez S., Clark S. E., Lopez-Rodriguez E., 2025, ApJ, 980, 197
Dale J. E., Ercolano B., Bonnell I. A., 2012, MNRAS, 424, 377
Dashyan G., Dubois Y., 2020, A&A, 638, A123
Davé R., Rafieferantsoa M. H., Thompson R. J., Hopkins P. F., 2017, MNRAS, 467, 115
Davé R., Anglés-Alcázar D., Narayanan D., Li Q., Rafieferantsoa M. H., Appleby S., 2019, MNRAS, 486, 2827
De Rossi M. E., Bower R. G., Font A. S., Schaye J., Theuns T., 2017, MNRAS, 472, 3354
Diesing R., Caprioli D., 2018, Phys. Rev. Lett., 121, 091101
Dome T., Martin-Alvarez S., Tacchella S., Yuan Y., Sijacki D., 2025, MNRAS, 537, 629
Dubois Y., Commerçon B., 2016, A&A, 585, A138
Dubois Y., Teyssier R., 2008, A&A, 482, L13
Dubois Y. et al., 2014, MNRAS, 444, 1453
Dubois Y., Commerçon B., Marcowith A., Brahimi L., 2019, A&A, 631, A121
Dubois Y. et al., 2021, A&A, 651, A109
Eldridge J. J., Izzard R. G., Tout C. A., 2008, MNRAS, 384, 1109
Emerick A., Bryan G. L., Mac Low M.-M., 2018, ApJ, 865, L22
Emerick A., Bryan G. L., Low M.-M. M., 2020, ApJ, 890, 155
Endsley R. et al., 2024, MNRAS, 533, 1111
Erb D. K., Shapley A. E., Pettini M., Steidel C. C., Reddy N. A., Adelberger K. L., 2006, ApJ, 644, 813
Evirgen C. C., Gent F. A., Shukurov A., Fletcher A., Bushby P. J., 2019, MNRAS, 488, 5065
Farcy M., Rosdahl J., Dubois Y., Blaizot J., Martin-Alvarez S., 2022, MNRAS, 513, 5000
Farcy M., Rosdahl J., Dubois Y., Blaizot J., Martin-Alvarez S., Haehnelt M., Kimm T., Teyssier R., 2025, A&A, 698, A89
Federrath C., Klessen R. S., 2012, ApJ, 761, 156
Ferland G. J., Peterson B. M., Horne K., Welsh W. F., Nahar S. N., 1992, ApJ, 387, 95
Fichtner Y. A., Mackey J., Grassitelli L., Romano-Díaz E., Porciani C., 2024, A&A, 690, A72
Fluetsch A. et al., 2019, MNRAS, 483, 4586
Fluetsch A. et al., 2021, MNRAS, 505, 5753
Ford A. B., Davé R., Oppenheimer B. D., Katz N., Kollmeier J. A., Thompson R., Weinberg D. H., 2014, MNRAS, 444, 1260
Forster Schreiber N. M. F. et al., 2019, ApJ, 875, 21
Fromang S., Hennebelle P., Teyssier R., 2006, A&A, 457, 371
Fu S. W. et al., 2024a, ApJ, 965, 36
Fu S. W. et al., 2024b, ApJ, 975, 2
Garrison-Kimmel S., Boylan-Kolchin M., Bullock J. S., Kirby E. N., 2014, MNRAS, 444, 222
Geen S., Hennebelle P., Tremblin P., Rosdahl J., 2015, MNRAS, 454, 4484
Geen S., Soler J. D., Hennebelle P., 2017, MNRAS, 471, 4844
Geha M., Blanton M. R., Yan R., Tinker J. L., 2012, ApJ, 757, 85
Geha M. et al., 2017, ApJ, 847, 4
Gelli V., Salvadori S., Pallottini A., Ferrara A., 2020, MNRAS, 498, 4134
Gentry E. S., Madau P., Krumholz M. R., 2020, MNRAS, 492, 1243
Girichidis P., Naab T., Hanasz M., Walch S., 2018, MNRAS, 479, 3042
Girichidis P., Pfrommer C., Pakmor R., Springel V., 2022, MNRAS, 510, 3917
Gorski K. M., Hivon E., Banday A. J., Wandelt B. D., Hansen F. K., Reinecke M., Bartelmann M., 2005, ApJ, 622, 759
Grønnow A., Tepper-García T., Bland-Hawthorn J., 2018, ApJ, 865, 64
Grudić M. Y., Guszejnov D., Hopkins P. F., Offner S. S., Faucher-Giguère C. A., 2021, MNRAS, 506, 2199
Grudić M. Y., Guszejnov D., Offner S. S., Rosen A. L., Raju A. N., Faucher-Giguère C. A., Hopkins P. F., 2022, MNRAS, 512, 216
Guo F., Oh S. P., 2008, MNRAS, 384, 251
Gutcke T. A., Pfrommer C., Bryan G. L., Pakmor R., Springel V., Naab T., 2022, ApJ, 941, 120
Hayward C. C., Hopkins P. F., 2017, MNRAS, 465, 1682
Heald G. H. et al., 2021, MNRAS, 509, 658
Heckman T. M., Alexandroff R. M., Borthakur S., Overzier R., Leitherer C., 2015, ApJ, 809, 147
Helder E. A., Vink J., Bamba A., Bleeker J. A., Burrows D. N., Ghavamian P., Yamazaki R., 2013, MNRAS, 435, 910
Hopkins P. F., Quataert E., Murray N., 2012, MNRAS, 421, 3522
Hopkins P. F. et al., 2018, MNRAS, 477, 1578
Hopkins P. F. et al., 2020, MNRAS, 492, 3465
Hopkins P. F., Chan T. K., Ji S., Hummels C. B., Kereš D., Quataert E., Faucher-Giguère C. A., 2021, MNRAS, 501, 3640
Hopkins P. F., Butsky I. S., Panopoulou G. V., Ji S., Quataert E., Faucher-Giguère C. A., Kereš D., 2022a, MNRAS, 516, 3470
Hopkins P. F., Squire J., Butsky I. S., Ji S., 2022b, MNRAS, 517, 5413
Jethwa P., Erkal D., Belokurov V., 2018, MNRAS, 473, 2060
Ji S., Oh O. P., McCourt M., 2018, MNRAS, 476, 852
Jubelgas M., Springel V., Enßlin T., Pfrommer C., 2008, A&A, 481, 33
Kado-Fong E. et al., 2024, ApJ, 966, 129
Katz H. et al., 2020, MNRAS, 494, 2200
Katz H. et al., 2021, MNRAS, 507, 1254
Katz H. et al., 2022, MNRAS, 515, 4265
Katz N., 1992, ApJ, 391, 502
Kereš D., Katz N., Weinberg D. H., Davé R., 2005, MNRAS, 363, 2
Kim C. G., Ostriker E. C., 2015, ApJ, 802, 99
Kim C.-G., Ostriker E. C., 2018, ApJ, 853, 173
Kim S. Y. et al., 2024, preprint (arXiv:2408.15214)

Kimm T., Cen R., 2014, ApJ, 788, 121
Kimm T., Cen R., Devriendt J., Dubois Y., Slyz A., 2015, MNRAS, 451, 2900
Kimm T., Katz H., Haehnelt M., Rosdahl J., Devriendt J., Slyz A., 2017, MNRAS, 466, 4826
Kirby E. N., Cohen J. G., Guhathakurta P., Cheng L., Bullock J. S., Gallazzi A., 2013, ApJ, 779, 102
Kocjan Z., Cadiou C., Agertz O., Pontzen A., 2024, MNRAS, 534, 918
Körtgen B., Banerjee R., Pudritz R. E., Schmidt W., 2019, MNRAS, 489, 5004
Koudmani S., Sijacki D., Smith M. C., 2022, MNRAS, 516, 2112
Krause M. et al., 2020, A&A, 639, A112
Krumholz M. R. et al., 2014, in Beuther H., Klessen R. S., Dullemond C. P., Henning T., eds, Protostars and Planets VI, Star Cluster Formation and Feedback. University of Arizona Press, Tucson, AZ, p. 243
Lee J., Kimm T., Blaizot J., Devriendt J., Martin-Alvarez S., Rhee J., Rey M., Slyz A., 2025, preprint (arXiv:2507.03127)
Leroy A. K. et al., 2015, ApJ, 814, 83
Li F. et al., 2020, MNRAS, 500, 1038
Llerena M. et al., 2023, A&A, 676, A53
Looser T. J. et al., 2024, Nature, 629, 53
Lopez-Rodriguez E., 2023, ApJ, 953, 113
Lopez-Rodriguez E., Guerra J. A., Asgari-Targhi M., Schmelz J. T., 2021, ApJ, 914, 24
Lopez-Rodriguez E. et al., 2023, ApJ, 942, L13
Maglione D., Martin-Alvarez S., Lopez-Rodriguez E., Clark S. E., Karpovich K., 2025, J. Astron. Telesc. Instrum. Syst., 11, 031620
Marasco A. et al., 2023, A&A, 670, A92
Martin-Alvarez S., Devriendt J., Slyz A., Teyssier R., 2018, MNRAS, 479, 3343
Martin-Alvarez S., Slyz A., Devriendt J., Gómez-Guijarro C., 2020, MNRAS, 495, 4475
Martin-Alvarez S., Katz H., Sijacki D., Devriendt J., Slyz A., 2021, MNRAS, 504, 2517
Martin-Alvarez S., Sijacki D., Haehnelt M. G., Farcy M., Dubois Y., Belokurov V., Rosdahl J., Lopez-Rodriguez E., 2023, MNRAS, 525, 3806
Martin-Alvarez S. et al., 2024, ApJ, 966, 43
Martin-Alvarez S., Sijacki D., Haehnelt M., Dubois Y., Rosdahl J., 2025, American Astronomical Society Meeting Abstracts Vol. 245, AmericanAstronomical Society Meeting Abstracts #245, 240.04
Martizzi D., Faucher C.-A., Ere G., Quataert E., 2015, MNRAS, 450, 504
McQuinn K. B., van Zee L., Skillman E. D., 2019, ApJ, 886, 74
Menon S. H., Federrath C., Krumholz M. R., 2023, MNRAS, 521, 5160
Mezcua M., Civano F., Fabbiano G., Miyaji T., Marchesi S., 2016, ApJ, 817, 20
Morlino G., Caprioli D., 2012, A&A, 538, A81
Naab T., Ostriker J. P., 2017, Annu. Rev. Astron. Astrophys, 55, 59
Nuñez-Castiñeyra A., Grenier I. A., Bournaud F., Dubois Y., Youssef F. R. K., Hennebelle P., 2022, preprint(arXiv:2205.08163)
Ocvirk P., Pichon C., Teyssier R., 2008, MNRAS, 390, 1326
Oñorbe J., Boylan-Kolchin M., Bullock J. S., Hopkins P. F., Kereš D., Faucher-Giguère C. A., Quataert E., Murray N., 2015, MNRAS, 454, 2092
Padoan P., Nordlund A., 2011, ApJ, 730, 40
Pakmor R., Pfrommer C., Simpson C. M., Springel V., 2016, ApJ, 824, L30
Parizot E., Marcowith A., Ballet J., Gallant Y. A., 2006, A&A, 453, 387
Pavičević M., Iršič V., Viel M., Bolton J. S., Haehnelt M. G., Martin-Alvarez S., Puchwein E., Ralegankar P., 2025, Phys. Rev. Lett., 135, 071001
Pfrommer C., Enßlin T. A., Springel V., Jubelgas M., Dolag K., 2007, MNRAS, 378, 385
Pfrommer C., Pakmor R., Schaal K., Simpson C. M., Springel V., 2017a, MNRAS, 465, 4500
Pfrommer C., Pakmor R., Simpson C. M., Springel V., 2017b, ApJ, 847, L13
Pillepich A. et al., 2018, MNRAS, 473, 4077
Ponnada S. B. et al., 2024, MNRAS, 530, L1
Power C., Navarro J. F., Jenkins A., Frenk C. S., White S. D. M., Springel V., Stadel J., Quinn T., 2003, MNRAS, 338, 14
Prochaska J. X. et al., 2017, ApJ, 837, 169
Rasera Y., Teyssier R., 2006, A&A, 445, 1
Rey M. P., Pontzen A., Agertz O., Orkney M. D., Read J. I., Rosdahl J., 2020, MNRAS, 497, 1508
Robinson H., Wadsley J., 2024, MNRAS, 534, 1420
Rodríguez Montero F., Martin-Alvarez S., Sijacki D., Slyz A., Devriendt J., Dubois Y., 2022, MNRAS, 511, 1247
Rodríguez Montero F., Martin-Alvarez S., Slyz A., Devriendt J., Dubois Y., Sijacki D., 2024, MNRAS, 530, 3617
Romano M. et al., 2023, A&A, 677, A44
Rosdahl J., Teyssier R., 2015, MNRAS, 449, 4380
Rosdahl J., Blaizot J., Aubert D., Stranex T., Teyssier R., 2013, MNRAS, 436, 2188
Rosdahl J., Schaye J., Teyssier R., Agertz O., 2015, MNRAS, 451, 34
Rosdahl J., Schaye J., Dubois Y., Kimm T., Teyssier R., 2017, MNRAS, 466, 11
Rosdahl J. et al., 2018, MNRAS, 479, 994
Rosdahl J. et al., 2022, MNRAS, 515, 2386
Rupke D. S., Veilleux S., Sanders D. B., 2005, ApJS, 160, 115
Salem M., Bryan G. L., 2014, MNRAS, 437, 3312
Salem M., Bryan G. L., Corlies L., 2016, MNRAS, 456, 582
Sanati M., Revaz Y., Schober J., Kunze K. E., Jablonka P., 2020, A&A, 643, 54
Sanati M., Martin-Alvarez S., Schober J., Revaz Y., Slyz A., Devriendt J., 2024, A&A, 690, A59
Santistevan I. B., Wetzel A., El-Badry K., Bland-Hawthorn J., Boylan-Kolchin M., Bailin J., Faucher-Giguère C. A., Benincasa S., 2020, MNRAS, 497, 747
Sartorio N. S., Vandenbroucke B., Falceta-Goncalves D., Wood K., 2020, MNRAS, 500, 1833
Sawala T. et al., 2016, MNRAS, 457, 1931
Schaye J. et al., 2015, MNRAS, 446, 521
Schmidt M., 1959, ApJ, 129, 243
Schneider R., Omukai K., Bianchi S., Valiante R., 2012, MNRAS, 419, 1566
Schroetter I. et al., 2019, MNRAS, 490, 4368
Schroetter I. et al., 2021, MNRAS, 506, 1355
Schruba A. et al., 2012, AJ, 143, 138
Shen X. et al., 2025, preprint (arXiv:2503.01949)
Shimizu I., Todoroki K., Yajima H., Nagamine K., 2019, MNRAS, 484, 2632
Shukurov A., Evirgen C. C., Fletcher A., Bushby P. J., Gent F. A., 2018, Technical Report, Magnetic Field Effects on the ISM Structure and Galactic Outflows, preprint (arXiv:1810.01202)
Simpson C. M., Pakmor R., Pfrommer C., Glover S. C. O., Smith R., 2023, MNRAS, 520, 4621
Smith M. C., Sijacki D., Shen S., 2018, MNRAS, 478, 302
Smith M. C., Sijacki D., Shen S., 2019, MNRAS, 485, 3317
Smith M. C., Bryan G. L., Somerville R. S., Hu C. Y., Teyssier R., Burkhart B., Hernquist L., 2021, MNRAS, 506, 3882
Springel V., Hernquist L., 2003, MNRAS, 339, 312
Stanway E. R., Eldridge J. J., Becker G. D., 2016, MNRAS, 456, 485
Steidel C. C., Erb D. K., Shapley A. E., Pettini M., Reddy N., Bogosavljević M., Rudie G. C., Rakic O., 2010, ApJ, 717, 289
Stein M. et al., 2025, A&A, 696, A112
Stein Y. et al., 2020, A&A, 639, A111
Stern J., Hennawi J. F., Prochaska J. X., Werk J. K., 2016, ApJ, 830, 87
Strickland D. K., Stevens I. R., 2000, MNRAS, 314, 511
Strickland D. K., Heckman T. M., Colbert E. J. M., Hoopes C. G., Weaver K. A., 2004, ApJS, 151, 193
Taziaux S. et al., 2025, A&A, 696, A226
Teyssier R., 2002, A&A, 385, 337
Teyssier R., Fromang S., Dormy E., 2006, J. Comput. Phys., 218, 44
Teyssier R., Pontzen A., Dubois Y., Read J. I., 2013, MNRAS, 429, 3068
Thomas T., Pfrommer C., Pakmor R., 2023, MNRAS, 521, 3023
Thornton K., Gaudlitz M., Janka H.-T., Steinmetz M., 1998, ApJ, 500, 95
Torrey P. et al., 2019, MNRAS, 484, 5587
Tremonti C. A. et al., 2004, ApJ, 613, 898
Tumlinson J. et al., 2011, Science, 334, 948

Tumlinson J., Peeples M. S., Werk J. K., 2017, ARA&A, 55, 389
Tweed D., Devriendt J., Blaizot J., Colombi S., Slyz A., 2009, A&A, 506, 647
Van De Voort F., Bieri R., Pakmor R., Gómez F. A., Grand R. J., Marinacci F., 2021, MNRAS, 501, 4888
Veilleux S., Cecil G., Bland-Hawthorn J., 2005, ARA&A, 43, 769
Veilleux S., Maiolino R., Bolatto A. D., Aalto S., 2020, A&AR, 28, 2
Vogelsberger M. et al., 2014, MNRAS, 444, 1518
Vogelsberger M., Marinacci F., Torrey P., Puchwein E., 2020, Nat. Rev. Phys., 2, 42
Walch S., Naab T., 2015, MNRAS, 451, 2757
Werk J. K. et al., 2014, ApJ, 792, 8
Werk J. K. et al., 2016, ApJ, 833, 54
White S. D. M., Rees M. J., 1978, MNRAS, 183, 341
Wise J. H., Turk M. J., Norman M. L., Abel T., 2012, ApJ, 745, 50
Witten C. et al., 2024, Nat. Astron., 8, 384
Witten C. et al., 2025, MNRAS, 537, 112
Yamasaki N. Y., Sato K., Mitsuishi I., Ohashi T., 2009, PASJ, 61, S291
Yang H. et al., 2017a, ApJ, 844, 171
Yang H., Malhotra S., Rhoads J. E., Wang J., 2017b, ApJ, 847, 38
Yuan Y., Martin-Alvarez S., Haehnelt M. G., Garel T., Sijacki D., 2024, MNRAS, 532, 3643
Yuan Y., Martin-Alvarez S., Haehnelt M. G., Garel T., Keating L., Witstok J., Sijacki D., 2025, MNRAS, 542, 762
Zahid H. J., Geller M. J., Kewley L. J., Hwang H. S., Fabricant D. G., Kurtz M. J., 2013, ApJ, 771, L19
Zamora-Avilés M., Vázquez-Semadeni E., Körtgen B., Banerjee R., Hartmann L., 2018, MNRAS, 474, 4824
Zheng Y. et al., 2024, ApJ, 960, 55

APPENDIX A: ON THE COMPUTATION OF THERMAL AND NON-THERMAL PRESSURE COMPONENTS

We compute the standard thermal pressure assuming an ideal gas law:

$$P_{\rm th} = (\gamma - 1)\,\rho_{\rm gas}\epsilon, \tag{A1}$$

where ϵ represents the internal energy per unit mass, and assuming a $\gamma = 5/3$ corresponding to a monoatomic ideal gas.

For the magnetic pressure, we assume an isotropic force distribution, estimated simply as

$$P_{\rm B} = \frac{B^2}{8\pi}, \tag{A2}$$

and where B is the total strength of the magnetic field.

The CR pressure is also accessible in our models with CRs the simulation, computed as

$$P_{\rm CR} = (\gamma_{\rm CR} - 1)\,e_{\rm CR}. \tag{A3}$$

Here, $e_{\rm CR}$ is the CR energy density, with $\gamma_{\rm CR} = 4/3$ corresponding to a relativistic fluid. To explore the importance of radiation, we follow J. Rosdahl et al. (2015) and estimate the photoheating pressure $p_{\rm photoheat}$ due to the photoionization of the hydrogen gas

$$\frac{p_{\rm photoheat}}{\rho_{\rm gas} k_{\rm B}} \sim T^{\rm ph} \sim 2\times10^4\,{\rm K}\,\min\left(f_{\rm vol}, 1\right), \tag{A4}$$

where $f_{\rm vol}$ is the fraction of the cell volume that is covered by the Strömgrem sphere with Strömgrem radius r_S

$$f_{\rm vol} = \frac{1}{(\Delta x)^3}\frac{4\pi r_S^3}{3} = \frac{1}{(\Delta x)^3}\frac{4\pi}{3}\frac{3\hat{L}_{\rm UV}}{4\pi\alpha^B n_H^2}, \tag{A5}$$

with n_H the hydrogen number density and $\alpha^B = 2.6\times10^{-13}$ cm^3 sec^{-1} the case B recombination of hydrogen for $T\sim 2\times10^4$ K (G. J. Ferland et al. 1992). To measure $f_{\rm vol}$ for a given cell, we approximate the UV photon luminosity $\hat{L}_{\rm UV}$ by using the ionizing photons density $\hat{\epsilon}_{\rm UV}$ in flux units. Thus equation (A5) becomes

$$f_{\rm vol} = \frac{1}{\Delta x}\frac{4\pi}{3}\frac{3\,c\,\hat{\epsilon}_{\rm UV}}{4\pi\alpha^B n_H^2}, \tag{A6}$$

where c is the speed of light. We also follow J. Rosdahl et al. (see their section 4.2.2; 2015) to estimate the direct pressure from photoionization ($p_{\rm UV}$) using again the same approximation for $\hat{L}_{\rm UV}$. However, we do not include it in our profiles as we find it to be negligible at these radial scales ($p_{\rm UV} \ll 10^{-30}$ erg cm^{-3}), in agreement with previous works (J. Rosdahl et al. 2015; A. Emerick, G. L. Bryan & M.-M. M. Low 2020). Note that this pressure might still be important in the regulation of star formation at smaller scales (J. H. Wise et al. 2012).

APPENDIX B: ON THE VARIABILITY OF PROPERTIES ACROSS TIME

Given the variability of galaxy internal properties across their evolution, and specifically with their star formation activity, in this appendix we provide additional context for interpreting the conditions described in the main text. Specifically, we compare the radial profiles at a given time to time-aggregated profiles. While these aggregates do not represent any specific single physical state, they describe the range and variability of conditions over time. This is particularly insightful when separated on to quiescent and star-forming subsets, with the star-forming being of particular interest for our study.

Fig. B1 shows the median radial pressure profiles averaging over time (solid curves) and their 1σ (16–84$^{\rm th}$, shaded bands) envelopes. The top panel shows the standard hydrodynamics model (HD) across the redshift interval $z\in[5.0,\ 3.4]$. The panel also shows the individual thermal pressure profiles as thin grey lines. Overall, the shaded band is relatively narrow, and captures well the variability of the profiles over time, with only individual peaks corresponding to satellites and companions deviating from this range. This is in agreement with a relatively continued star formation activity over time, approximately self-regulated by SN feedback. Due to the large burstiness of the RTCRiMHD model, the model exhibits different conditions depending on the star formation rate of the galaxy. We show the profiles during either high sSFR (star-forming, sSFR >1 Gyr^{-1}; central panel) or low sSFR (quiescent; bottom panel) periods. Overall, and focusing on the high sSFR period, we recover the main trends described in the main text. The non-thermal profiles exhibit wider envelopes than the thermal pressure, reflecting the higher variability of these components. This is especially notable for the magnetic energy, which only globally dominates at times in the innermost regions of the galaxy. Photoheating and cosmic rays remain subdominant in the galaxy, with their upper end of the 1σ bands comparable to the thermal pressure distribution. CRs and photoheating pressures are comparable to the thermal pressure at $r>1$ kpc, with photoheating dominating at large radii. The CR pressure bands reflect the discussed trend for this component to, at times, dominate the pressure of outflowing gas. Effectively, the CR pressure is comparable to (and overtakes at times) the thermal pressure in the 1 kpc $\lesssim r \lesssim$ 4 kpc range. The scaling of the median CR pressure in the $r\in[2,\ 15]$ kpc regime is relatively insensitive to removing outflowing gas in the computation of this pressure, and remains approximately $\propto r^{-2} - r^{-3}$ Finally, during times of relative quiescence (sSFR <1 Gyr^{-1}), all pressures in the galaxy fall well below the HD profiles. While this drop is partially driven by

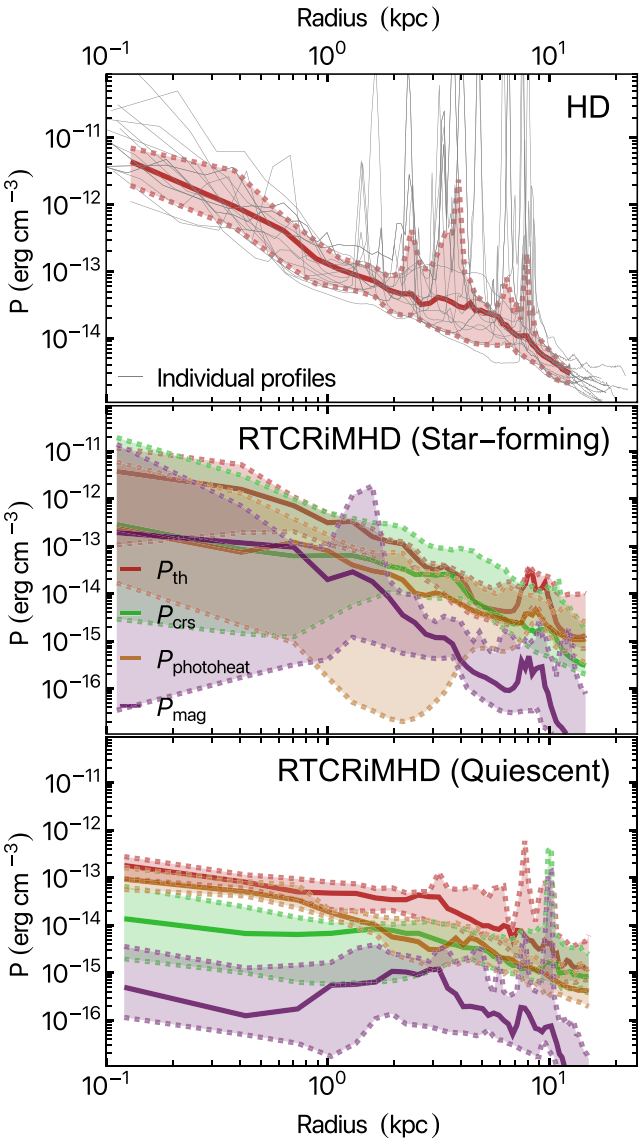

Figure B1. Median radial pressure profiles within the interval $z \in [5.0, 3.5]$, shown as thick coloured curves. Shaded regions indicate the 16–84$^{\text{th}}$ percentiles. The panels, from top to bottom, show: (top) the HD model, (centre) the full-physics model during high star formation periods, and (bottom) the full-physics run during quiescent periods. Pressure components are thermal (P_{th}, red), cosmic-ray (P_{crs}, green), photoheating ($P_{\text{photoheat}}$, orange), and magnetic (P_{mag}, purple). We include as thin grey lines in the HD panel, P_{th} profiles for each snapshot. The Fig. 4 snapshots are within the 1σ bands of the HD panel, and of the star-forming RTCRiMHD panel. The only deviations appear in peaks corresponding to satellite galaxies.

lower gas densities, we also find a relative drop in the non-thermal pressures contribution with respect to the thermal component. During these episodes, only the photoheating pressure remains important in the galaxy. At large radii, photoheating and CRs are comparable, and can contribute a non-negligible fraction of the total pressure. Magnetic energies remain subdominant globally, although we note that they are still locally important in some dense regions within the galaxy. Overall, while individual snapshots may feature profiles with small variations of the pressure distributions, the profiles studied in Fig. 4, and their main results are representative of the typical radial distribution of pressures, specifically during times of non-negligible star formation.

APPENDIX C: BROAD VELOCITY COMPONENT MEASUREMENTS AS A PROXY FOR GALAXY OUTFLOWS

In this appendix, we provide additional information regarding our observation-like measurements of galaxy outflows. We adopt a simple approach to illustrate the potential impact of more sophisticated forward-modelling. Our method, following the observational procedure, is based on extracting information from the velocity distribution, which can be recovered observationally by studying emission line velocity profiles. Specifically, a common technique is to decompose emission line profiles into two Gaussian contributions, with the narrow component associated with the galaxy, and the broad component associated the galaxy's outflow (e.g. D. S. Rupke et al. 2005; A. Marasco et al. 2023; M. Romano et al. 2023; S. Carniani et al. 2024). The information about this broad component can be used to calculate the two main parameters required to estimate an outflow rate using equation (1). These are the outflow velocity, v_{broad}, which is primarily connected with the FWHM of the Gaussian component, and the outflow mass, M_{outflow}, which is affected by both its FWHM and its amplitude.

To extract the broad component information from our simulations, we obtain for each snapshot the cumulative mass (or $L_{\text{H}\,\alpha}$) distribution function for the line-of-sight velocities across 12 directions. These are equidistantly distributed following a HEALPIX sphere discretization (K. M. Gorski et al. 2005). When computing the mass distribution function, gas cells contributing to this mass distribution function are filtered accordingly to whether the WIM or WNM component is being considered. We include in this calculation only cells within a distance less than $r < 0.1\, r_{\text{halo}}$. We attempt both a fit with a single and a double Gaussian function. For the gas mass distribution functions, we determine whether the double Gaussian decomposition is valid following a simple Akaike Information Criterion (AIC), and discard the double Gaussian fit when it provides:

$$\text{AIC}_{\text{double}} < \text{AIC}_{\text{single}} - 2. \tag{C1}$$

Due to the lower fraction of valid fits in our H α analysis, we relax this assumption to simply yielding at least a 10 per cent reduction of sum of squared residuals (SSR). We discard snapshots where the double Gaussian decomposition is invalid.

In Fig. C1 we show an example of the double Gaussian fit for the WIM velocity distribution of the RTCRiMHD model. It reflects how the broad component of the double Gaussian fit is able to capture the outflowing WIM mass (red histogram). This decomposition appears to be valid for our dwarf galaxies due to the relative isotropy of their outflows, although we note that inclination with respect to a face-on viewing line may be important for galaxies with coherent rotation (A. Concas et al. 2022) and/or more complex outflow morphologies.

The first quantity we extract from the broad component is the outflow velocity, v_{broad}. This is typically interpreted as an observational proxy for the 95$^{\text{th}}$ percentile of the velocity distribution. Still following the methodology from observational studies, we compute v_{broad} as described by equation (2). To determine how this velocity relates to the high-velocity tail of the outflows in our simulations, we compare it with $v_{95\ \text{per cent}}$. We measure $v_{95\ \text{per cent}}$ directly, as the velocity marking the 95$^{\text{th}}$ percentile of the mass-weighted velocity distribution. These two velocities are compared in the top panel of Fig. C2 for the WIM component, although we note that the WNM displays a similar relation. Overall, the v_{broad} traces the $v_{95\ \text{per cent}}$

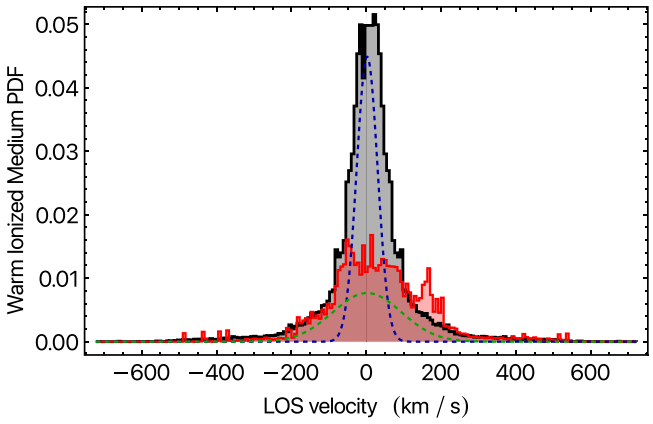

Figure C1. Sample LOS velocity distribution of WIM mass for a RTCRiMHD model output (also shown in Fig. 1) with a valid double Gaussian fit. Black and red histograms show all WIM gas and the outflowing component, respectively. The dashed blue and green lines show the narrow and broad Gaussian fits. The broad component effectively captures the outflowing gas, due to its roughly isotropic morphology.

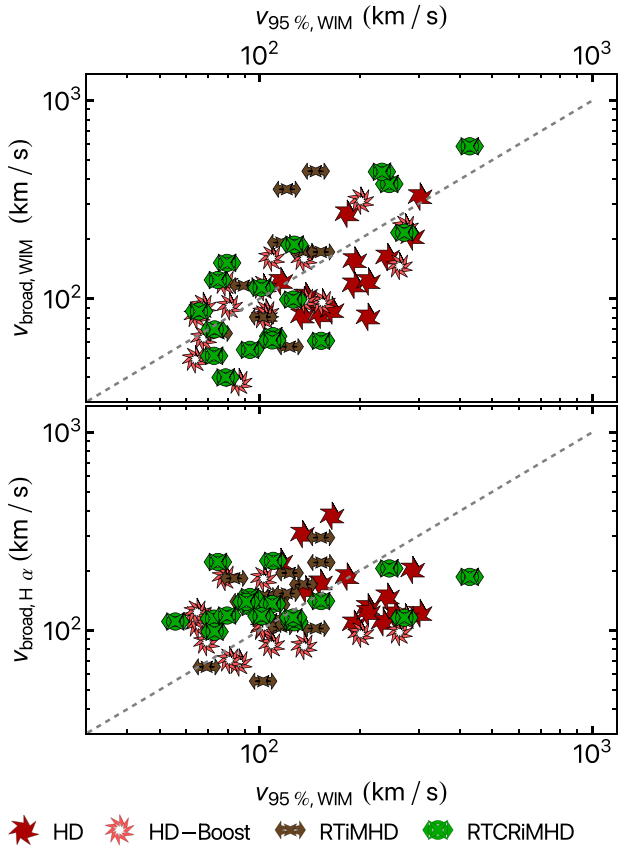

Figure C2. Top panel: Relation between the broad velocity estimate for high-velocity outflows, v_{broad}, and the mass-weighted velocity of gas with speeds above the 95$^{\mathrm{th}}$ percentile. Bottom panel: Same as the top panel, now employing the H α luminosity distribution of velocities to measure the broad velocity estimate. The relatively tight correlation between these two quantities suggests that v_{broad} is a reasonable tracer of the $v_{95\ \mathrm{per\ cent}}$.

reasonably well, and does not display any particular bias for any of our models. As a result, we employ v_{broad} in our main analysis, which enables a more direct comparison across our observation-like results as well as with the observational ones. The bottom panel of the same figure compares $v_{95\ \mathrm{per\ cent}}$ with $v_{\mathrm{H}\,\alpha,\,\mathrm{broad}}$, which displays a similar correlation, although with a somewhat larger scatter, and with the highest velocities somewhat underestimated. Understanding why this is the case will require a larger sample of simulated galaxies. Velocity measurement variations are relatively small across our models, suggesting that for an individual galaxy, the uncertainty associated with the broad velocity does not significantly bias the measurement of the outflow rate, even for potentially large variations in physical modelling. Despite this, we note that, as discussed in the main text, v_{broad} (and $v_{95\ \mathrm{PLXDEL}}$%PLXINS per cent) is biased high when compared with the mass-weighted velocity of the outflowing gas frequently employed by simulations. Employing a luminosity-weighted value for the outflow velocity instead of using $v_{95\ \mathrm{PLXDEL\%PLXINS}\ \textit{per cent}}$ would likely decrease the estimated outflow rate by ~ 1 dex.

Estimating the outflowing mass is more challenging observationally, even when assuming that the broad component amplitude is well-recovered. Specifically, estimating the outflow mass requires of approximations such as those adopted in equation (3), where the electron number densities frequently cannot be directly inferred from (dwarf) galaxy observations. Instead, this is often set to $n_e \sim 300\,\mathrm{cm}^{-3}$ as an extrapolation of the values retrieved from more massive galaxies and/or AGN-outflows. This measurement often relies on the [S II]λ6717Å/[S II]λ6731Å intensity ratio narrow sensitivity range ($100 - 2000\,\mathrm{cm}^{-3}$; D. Baron et al. 2024). Dwarf galaxy formation simulations such as those studied here typically feature lower average SN-driven outflow densities, of the order of a few H cm^{-3}, and have clear density gradients. Assuming a comparable electron number density would lead to an increase of outflow mass rates estimates of $\sim 1 - 3$ dex.

From the observational side, a potential avenue to further bridge the gap between the methods typically employed by numerical simulations and observations would be assuming $n_e \sim 1\,\mathrm{cm}^{-3}$, and measuring the outflow velocity as the amplitude-weighted norm of the velocity relative to the mean of the broad component. From the numerical side, our findings indicate that additional work addressing detailed forward-modelling of the outflow properties of simulated dwarf galaxies – especially leveraging a larger galaxy samples – will be fundamental to interpret the importance of these caveats, and establish a direct connection between the properties of simulated and observed outflows.

APPENDIX D: THE MASS–METALLICITY RELATION ACROSS ALL PANDORA MODELS

In this appendix, we provide additional results for the mass–metallicity relation in the Pandora simulations in Fig. D1. The top panel of the figure displays, for completeness, the mass–metallicity relation as measured for all the Pandora models. The bottom panel shows the models that are evolved closer to $z = 0$ to underscore how the studied galaxy does not evolve further in the mass–metallicity space. Overall, the mass–metallicity relation for the additional models reinforces the conclusions discussed above. While the simulations employing a density threshold star formation model (NoFb + thSf, HD + thSf, and HD + thSf Boost) have important effects across various other galaxy properties (S. Martin-Alvarez et al. 2023), their final metallicities are comparable to their MTT star formation model counterparts (NoFb, HD, and HD + Boost, respectively). The

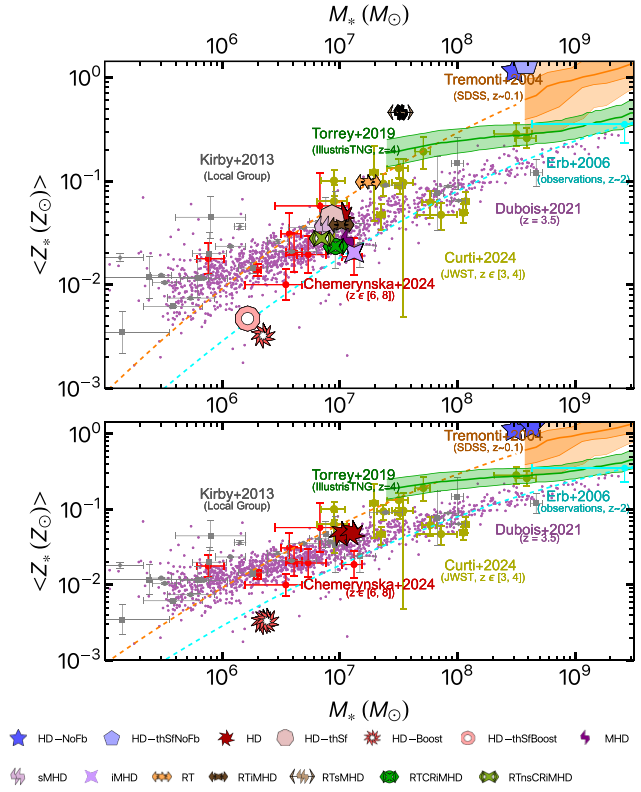

Figure D1. Top panel: Stellar mass–stellar metallicity relation, as shown in Fig. 9, now for all the Pandora dwarf galaxy simulated models. As in Fig. 9, we include for comparison local dwarf galaxies stellar metallicity observations (grey points) by E. N. Kirby et al. (2013) and higher redshift observations employing *JWST* by M. Curti et al. (2024) at $z \in [3, 4]$ (yellow points) and I. Chemerynska et al. (2024) at $z \in [6, 8]$ (red points). We include larger stellar masses *SDSS* observations at low (C. A. Tremonti et al. 2004; orange bands) and high ($z \sim 2$; D. K. Erb et al. 2006) redshift (cyan points and cyan dashed line). We also show data for the high-resolution New Horizon ($z = 3.5$, violet data points; Y. Dubois et al. 2021) and IllustrisTNG ($z = 4$, green band; P. Torrey et al. 2019) simulations for comparison. Most models provide a reasonable match to observations, except the 'boosted' feedback model HD + Boost. Bottom panel: Same as the top panel, but now for the NoFb, HD, and HD + Boost models at both $z \sim 3.5$ and $z \sim 0.5$, to showcase the lack of evolution after the main studied period.

inclusion of magnetic fields (MHD, iMHD) leads only to a minor variation in metallicity with respect to the standard hydrodynamical models (HD + thSf and HD). Their overall metallicity is slightly reduced as star formation becomes more concentrated (S. Martin-Alvarez et al. 2020), and the subsequent galactic outflows have a higher proportion of entrained metals, in an analogous manner to the HD + thSf Boost and HD + Boost models. In the model with stellar radiation in the absence of magnetic fields (RT), a lower concentration of star formation only weakens the role of stellar feedback and leads to both a higher mass and stellar metallicity. S. Martin-Alvarez et al. (2023) described how various relations show that extreme primordial magnetizations (comparable or 1 dex below non-CMB constraints; H. Katz et al. 2021; M. Pavičević et al. 2025 – see also A. E. Broderick et al. 2018) are disfavoured by the Pandora simulations in the presence of stellar radiation. We find this same apparent disagreement with both local and high redshift dwarf galaxies (E. N. Kirby et al. 2013; M. Curti et al. 2024). Finally, the *'full-physics'* model without CR streaming (RTnsCRiMHD) features a comparable metallicity to the studied RTCRiMHD model, further supporting our main findings. Finally, focusing on the bottom panel of Fig. D1, we confirm that when evolved closer to $z = 0$, the Pandora galaxy undergoes very minor evolution in its stellar mass–metallicity relation. This lack of evolution holds regardless of the strength of stellar feedback, with the three displayed models spanning from 'boosted' SN feedback to a model with no stellar feedback (only gas and metals mass return to the ISM), and matches the expectation for a very isolated dwarf galaxy with minor evolution and no additional mergers (see appendix A by S. Martin-Alvarez et al. 2023)

This paper has been typeset from a TEX/LATEX file prepared by the author.